Machine Control System Modeling and Design For Incremental Profile Forming of Metal Tubular Structures

Undergraduate Honors Research Thesis

Presented in Partial Fulfillment of the Requirements of Undergraduate Honors Research

By
Angella Volchko
Undergraduate Program in Mechanical Engineering

The Ohio State University
2019

Defense Committee:
Prof. Krishnaswamy Srinivasan, Advisor
Prof. Erman A. Tekkaya

Copyright by Angella Volchko, 2019.

Abstract

Today, manufacturers require specialized machinery to produce various metal tubular designs for aeronautical and automotive applications. In an effort to reduce machine and tooling redesign with every unique tubular cross-sectional profile, the Incremental Profile Forming (IPF) process was created a few years ago at the Technical University of Dortmund, Germany. The innovative IPF machine includes eight degrees of freedom of motion which enable flexibility in manufacturing, such that a single machine can produce various metal tube profiles. However, control of machine motions alone has not resulted in precision of the manufactured part geometry. The lack of precision using the current process calls for extending control of the manufacturing process beyond machine control, and for better utilization of machine control to support such extension. The purpose of this research is to investigate current control of machine motions used by the IPF machine, and identify ways to integrate machine control with process control to increase precision of the manufactured parts.

Within this research, the current machine control systems used to govern the motions of the radial actuators used for tube forming were studied. Multiple experiments were conducted on the IPF machine to help validate system models and investigate system responses to various inputs and IPF processes. The gathered force, position, and structural measurements were analyzed to support the development of the motion control system models, as well as active stiffness control and online identification methods. Extensions of the machine control to include active stiffness control and online-identification of process parameters are two different control methods that were investigated to help improve precision in tube manufacture. The potential of these two methods to better accommodate various process disturbances and process characteristics was examined.

Research results include complete models of the commercially available motors and radial actuators that are used by the motion control systems. These models were used to modify active stiffness control and online identification capabilities. This work establishes the basis for, and feasibility of, controller modeling for current and potential future functions performed by the IPF machine. Successful integration of new control methods in the IPF machine will enable effective use of its flexibility, while improving its accuracy in metal tube manufacturing.

Acknowledgements

I would like to thank Professor Cheena Srinivasan from The Ohio State University for his guidance and patience in my first take at the world of research. I would also like to thank Professor Tekkaya, as well as the IUL at the Technical University of Dortmund for welcoming us and allowing us to use their facility this past summer. I would also like to thank Agi Riskó for our German language instruction.

Table of Contents

List of Figures

List of Tables

Nomenclature

Parameter	**Symbol**	Value	Units
Equivalent Damping	b_{eq}	0.365	$N.m.s/rad$
Damping in Gearing	b_{gear}	0.010	$N.m.s/rad$
Damping of Motor	b_m	0.355	$N.m.s/rad$
Diameter of the Grooving Tool	d_{graver}	39	mm
Diameter of Lead Screw	d_{ls}	30	mm
Depth of Grooving Tool	D	$---$	mm
Radial Load Force Applied at Tool	F_L	$---$	N
Axial Backlash	h	0.08	mm
Current	i	$---$	A
Equivalent Inertia	J_{eq}	$2.219(10^{-4})$	$kg.m^2$
Inertia of the Graver and Screw	$J_{graverandscrew}$	$1.055(10^{-4})$	$kg.m^2$
Rotational Inertia of screw	J_{ls-rot}	$1.026(10^{-4})$	$kg.m^2$
Inertia of Motor	J_m	2.19	$kg.cm^2$
Phase to Phase Peak EMF Constant	$k_{e_{pkpk}}$	8.1528	$V.s$
Phase to Phase RMS EMF Constant	$k_{e_{RMS}}$	5.7649	$V.s$
Line to Line RMS EMF Constant	k_e	9.9851	$V.s$
Integral Gain of Velocity Loop	k_i	8699.57	V
Proportional Gain of Velocity Loop	k_p	7.2076	$V.s$
Proportional Gain of Position Loop	k_{pp}	313	s^{-1}
Stiffness Constant	k_v	$---$	rad/Nm

Parameter	**Symbol**	Value	Units
Kinetic Energy of Grooving Tool	KE_{graver}	$---$	J
Kinetic Energy of Lead Screw	KE_{ls}	$---$	J
Kinetic Energy of Lead Screw and Grooving Tool	$KE_{graverandscrew}$	$---$	J
Total Kinetic Energy of Graver System	KE_{total}	$---$	J
Length of the Grooving Tool	l_{graver}	400	mm
Length of Screw	l_{ls}	80	mm
Line to Line Inductance	L_{ll}	0.035812	H
Phase to Phase Inductance	L_{uv}	0.017906	H
Mass of the Grooving Tool	m_{graver}	3.687	kg
Mass of the Lead Screw	m_{ls}	0.912	kg
Gear Ratio	N	6	$---$
Pitch With Respect to Rotation of Lead Screw	p_{ls}	5	mm/rev
Pitch With Respect to Rotation of Motor	p_m	0.83	mm/rev
Radial Forming Force	P	$---$	N
Lifting Power	$P_{lifting}$	25	kN
Line to Line Resistance	R_{ll}	35.748	Ω
Phase to Phase Resistance	R_{uv}	17.874	Ω
Time	t	$---$	s
Output Torque	T	$---$	$N.m$
Load Torque	T_L	$---$	$N.m$

Parameter	**Symbol**	Value	Units
Idling Torque	T_0	0.15	$N.m$
Velocity of the Grooving Tool	v_{graver}	$----$	mm/s
Velocity of the Lead Screw	v_{ls}	$----$	mm/s
Input Voltage to Motor	V_{in}	$---$	V
Back EMF	V_{out} , e	$---$	V
Indentation Depth	δ	$---$	mm
Efficiency	η	0.55	$---$
Rotational Speed of Motor	ω	$---$	rad/s
Rotational Speed of Lead Screw	ω_{ls}	$---$	rad/s
Density of the Grooving Tool	ρ_{graver}	7715	kg/m^3
Density by Length of Screw	ρ_{ls}/l	1.14	$kg/100\,mm$
Flow Stress	σ	$----$	MPa
Rotational Position	θ	$----$	rad
Rotational Velocity	$\dot{\theta}$	$----$	rad/s
Rotational Acceleration	$\ddot{\theta}$	$----$	rad/s^2

1 Introduction to Incremental Profile Forming

1.1 Introduction to the Incremental Profile Forming Process and Context of Research

Many metal forming processes have been improved over the years to allow for flexible metallic manufacturing (Allwood et al., 2016). Flexibility can be defined as the capability of producing various metal parts with limited machining reconfiguration. Currently, there are no flexible manufacturing methods for lightweight load-adapted metallic tubular structures with appropriate cross-sectional profiles, which may be desired in automotive and aerospace applications. Current metal tubular forming processes rely on specialized machinery, a wide variety of tooling geometries, and multi-step processes to create desired tube configurations. The Incremental Profile Forming (IPF) process and machine were developed at the Technical University of Dortmund (TU Dortmund) to manufacture a variety of tubular cross-sectional profiles (Grzancic et al., 2014). The IPF machine and process flexibility is embedded in the eight degrees of freedom of motion incorporated in the design of the machine.

The eight degrees of freedom of the IPF machine are illustrated in Fig. 1.1.1. The IPF process functions by feeding metal tubes through a rotary disk via a hydraulic actuator, both of which actuate degrees of freedom for performing rotational and linear motions, respectively. A set of radial indenting actuators, called gravers, contact the tube, creating the intended structure. These six gravers make up the remaining six degrees of freedom of the IPF machine. This method, referred to as kinematic forming, can create over one hundred tubular cross-sectional profiles.

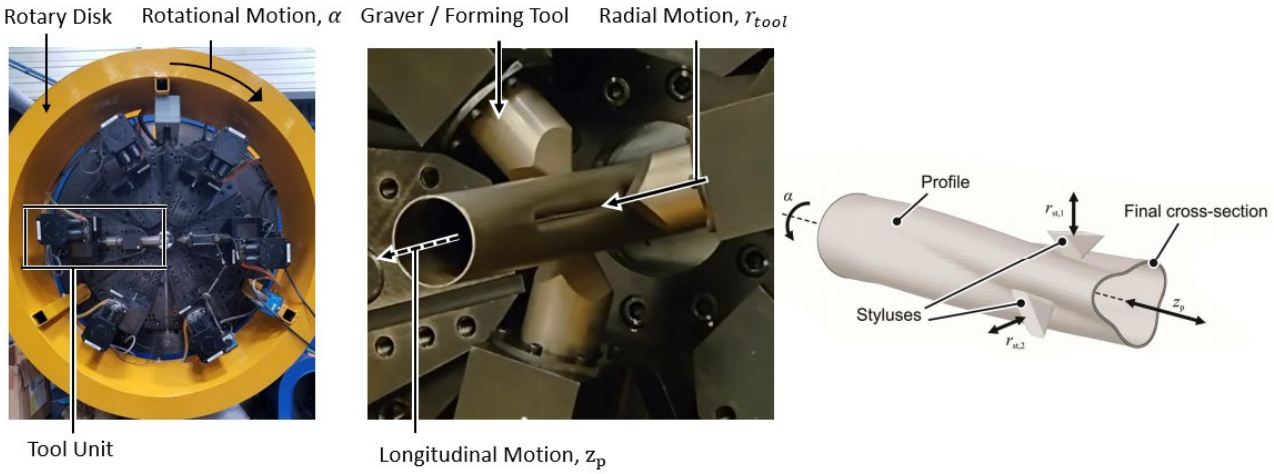

Figure 1.1.1 IPF process (Adapted from Grzancic et al., 2014)

This process, depicted in Fig. 1.1.1, needs to be improved, as control of machine motions alone does not consistently or precisely form the desired tube profile geometry. These defects arise, presumably, from limitations of both machine control and process response during and after process completion. The IPF process and its control need further development to better understand process mechanics and implement new system controls to accommodate process mechanics and ensure product geometry accuracy. Thus, although the machine is capable of producing multiple tube configurations with its innovative physical components, the geometrical accuracy of these designs will either require exhaustive trial and error methods or control systems that do not already exist within the machine. The purpose of this research is to model many of the current motion control systems and help support new IPF control methods to improve

product accuracy while retaining machine flexibility. Successful implementation of these control methods will increase precision in the IPF machine's manufactured products.

The process and parameters that are needed for simulation of the current machine control systems will be described. Two control methods will also be investigated: active stiffness control and online identification of material characteristics, along with the significance of their implementation for IPF process control.

The research efforts discussed here are part of a larger research effort to examine the entire IPF process to identify underlying causes and remedies required to ensure improved precision of the manufactured parts. Fig. 1.1.2 illustrates the control hierarchy for a general metal forming process, such as the IPF process. The outermost loop, the product property loop, accounts for accommodation of material properties at the microstructure level and their impact on product properties of interest. The middle loop, the process variable loop, accounts for the impact on the final tube geometry of process disturbances during indentation, such as non-uniform plastic strain, and of post-process disturbances, such as the recovery of elastic deformations once the indenting loads are removed. The innermost loop implements machine control: the motion and dynamics of the eight degrees of freedom including the hydraulic axial actuator, the rotary disk, and the six individual indenting motors. The machine control loop is certainly important for the precision of the process, and is the simplest to implement of the three control loops. The development and validation of the machine control loop specific to the indenting gravers will be the focus of the research. In addition, the potential of enhancing machine control to support the broader objectives of process control and product property control will be investigated.

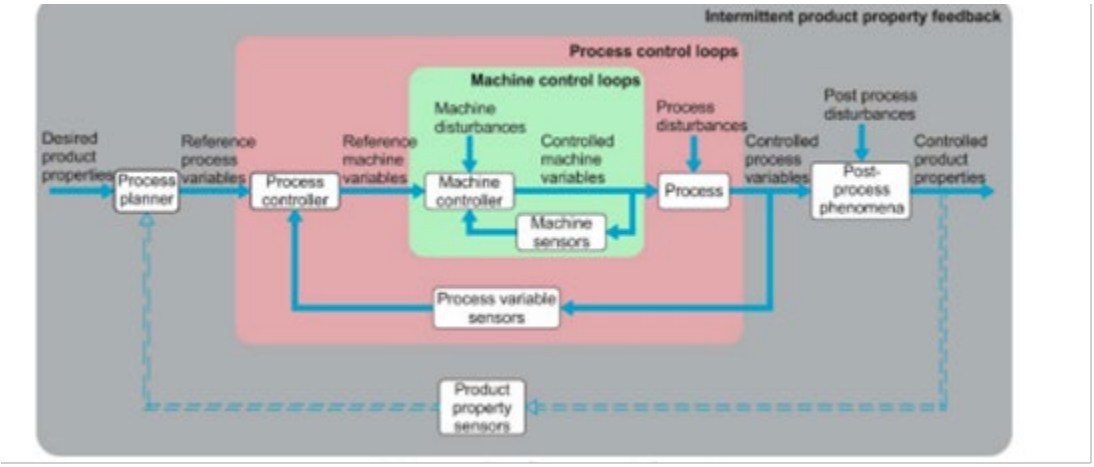

Figure 1.1.2 The three IPF process control loops (Srinivasan and Tekkaya, 2018)

The research described here involves the simulation, experimentation, and analysis pertaining to the machine control loops with respect to the graver dynamics and control. Fig. 1.1.2 is crucial to understanding the relationship of the research described here to the broader objectives of IPF process control. The structure of this thesis has been outlined by chapter to illustrate the flow of logic and content.

1.2 Thesis Outline

Chapter 2 describes the modeling and simulation of graver servo dynamics. The IPF gravers' controls, motors, dynamics, and mechanical transmission will be modeled. The necessary steps in the development of a Simulink model for a commercially available position-velocity controller and 3-phase brushless DC sinusoidal motor are described. External disturbances to the servo loop and their effect on the overall system response will also be modeled. The developed controllers will be modified to ensure improved execution of system commands, and their performance will be evaluated by computer simulation. Thus, a quantitative model of the innermost loop will be determined that should help researchers with development relating to the two outermost loops depicted in Fig. 1.1.2.

Chapter 3 describes experimental work, including the setup and equipment used to acquire force, position and tube geometry data during experimentation. Difficulties in implementing model validation and challenges presented by the current modes of control of the IPF machine will be described. Model predictions and experimental responses will be compared, and discrepancies identified.

Chapter 4 describes preliminary work in active stiffness control and online identification. The chapter discusses motivation behind both control methods to enhance some aspects of the IPF process response. The implementation of active stiffness control will be explored and what it means for the future development of the IPF machine with respect to the outer control loops in Fig. 1.1.2. This chapter also evaluates online process parameter identification opportunities and their implementation. Within this chapter, the potential of the IPF machine for online identification of process parameters will be identified along with implications for the outer loops of the process control hierarchy.

Chapter 5 states conclusions from the research and recommendations for future work. Implications of the work for future implementation of active stiffness control, as well as online identification of process parameters, will be described. Recommendations to address the limitations of the experimental work in Chapter 3 will also be listed, to ensure better validation of machine control system models.

2 Modeling and Simulation of the Graver Position Servomechanism

In this chapter, the dynamic response of the graver position servomechanism is modeled and studied using Simulink. The model and its simulation help identify servo limitations in response to commanded motion as well as the indenting forces. A dynamic model was originally created to identify the inaccuracy of the IPF process due to machine disturbances, and thus, separated from inaccuracies of the process due to other effects such as material deformation.

In addition, the dynamic model may be used to evaluate possible modifications of the graver control. A complete model of the graver servo dynamics will aid in appending new control methods. Since the physical model has been created, the controller and system dynamics of the process can be further investigated within a simulation obtaining parameters from the commercially distributed motors, transmission, and control system implemented in the IPF machine.

The simulation is necessary because each new controller design cannot feasibly be implemented on site until the design has been evaluated sufficiently to warrant hardware implementation.

2.1 Dynamic Model of Brushless Motor

First, the commercially available KEB motor of the IPF machine gravers was modeled. The TA 33 V30 ER TW motor was determined to be a 3 phase, 6 pole, brushless DC (BLDC) motor with stator windings in the star- or wye-configuration. All of these parameters were significant in modeling the dynamics of the motor accurately.

The graver motors are equipped with resolvers as the measurement device for position feedback, rather than the typical Hall Effect Sensors. The resolver is attached at the stator and provides the true rotational position of the motor, rather than a true tool position, since the mechanical transmission between the two are not completely robust.

Motor parameters used in determination of the dynamic model were provided in the documentation of the KEB BLDC motor. Motor parameters were documented as phase to phase values. A line to line conversion was made for each of these values to help simplify the analysis of the system. The phase to phase inductance, L_{uv}, and resistance, R_{uv}, were converted to their respective line to line values, L_{ll} and R_{uv}, in equation [2.1.1] and [2.1.2].

$$L_{ll} = 2 * L_{uv} \quad [2.1.1]$$

$$R_{ll} = 2 * R_{uv} \quad [2.1.2]$$

The provided phase to phase peak EMF constant, $k_{e_{pkpk}}$, was first converted to its equivalent phase to phase root mean square value, $k_{e_{RMS}}$, which was then converted to a line to line rms value, k_e, in equations [2.1.3] and [2.1.4]. The torque constant, k_t, could then be computed from the line to line rms emf constant [2.1.5] provided information that the BLDC motor is sinusoidal (Moreton, 1999).

$$k_{e_{RMS}} = \frac{k_{e_{pkpk}}}{\sqrt{2}} \quad [2.1.3]$$

$$k_e = \sqrt{3} * k_{e_{RMS}} \quad [2.1.4]$$

$$k_t = \sqrt{3} * k_e \quad [2.1.5]$$

Electrical and mechanical equations of the brushless DC motor [2.1.6 and 2.1.7] were created using the variables calculated in equations [2.1.1 - 2.1.5]. The electrical equation [2.1.6] relates the input voltage, V_{in}, the current, i, the resistance, $R_{ll,}$ the inductance, L_{ll}, and the back emf, V_{out}. The mechanical equation [2.1.7] relates the torque generated, T, the inertia of the motor, J_m, the rotational speed of the motor, ω_m, the damping of the motor, b_m, and the load torque acting at the motor, T_L. These two equations can be combined using the emf and torque constant relations provided in equation [2.1.8 and 2.1.9], to arrive at a simulation that specifies a certain motor speed given an input voltage.

$$V_{in} = R_{ll} i(t) + L_{ll} \frac{di}{dt}(t) + V_{out} \quad [2.1.6]$$

$$T = J_m \frac{d\omega}{dt}(t) + b_m \omega(t) + T_L \quad [2.1.7]$$

$$V = k_e \omega(t) \quad [2.1.8]$$

$$T = k_i i(t) \quad [2.1.9]$$

Equations [2.1.6] and [2.1.7] were rearranged and transformed into the Laplace domain as transfer functions [2.1.10 and 2.1.11] so they could be implemented into a Simulink block diagram.

$$\frac{I}{V_{in} - V_{out}} = \frac{1}{R_{ll} + L_{ll} s} \quad [2.1.10]$$

$$\frac{\omega}{T - T_L} = \frac{1}{b_m + J_m s} \quad [2.1.11]$$

Equations [2.1.8 - 2.1.11] were then compiled to create the following closed-loop system in Simulink, as depicted in Fig. 2.1.1.

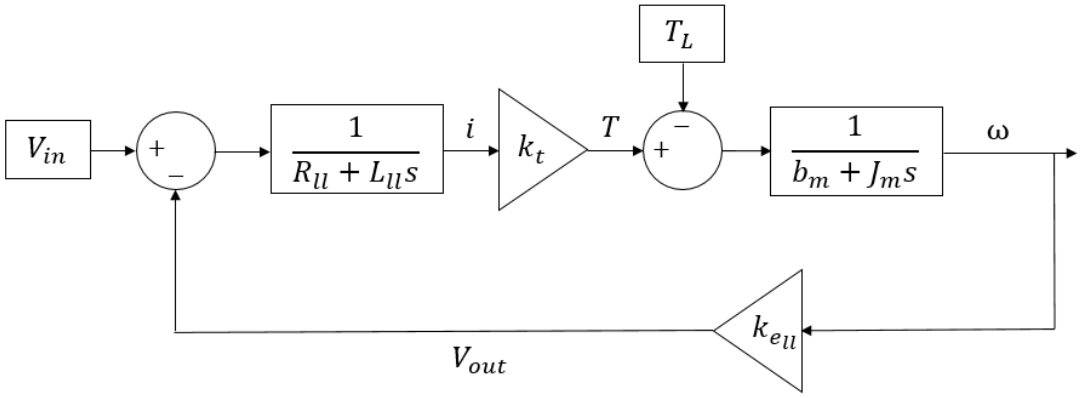

Figure 2.1.1 Closed loop block diagram of motor

The single closed-loop transfer function [2.1.12] describing the output of motor speed given a specified input voltage could then easily be constructed from the motor dynamics block diagram (Fig. 2.1.1).

$$\frac{\omega}{V_{in}} = \frac{k_t}{L_{ll} J s^2 + (R_{ll} J + L b_m) s + k_{e_{ll}} k_t + R_{ll} b_m} \quad [2.1.12]$$

The simplified transfer function using the line to line parameters will be used in analysis and design of the IPF graver controls.

2.2 Mechanical Transmission System Model

The dynamics of the mechanical transmission must be captured in the simulated model. The graver is equipped with an ANT ball screw worm gear model NM3-V which converts rotational motion of the motor into linear actuation of the tool, as depicted in Fig. 2.2.1.

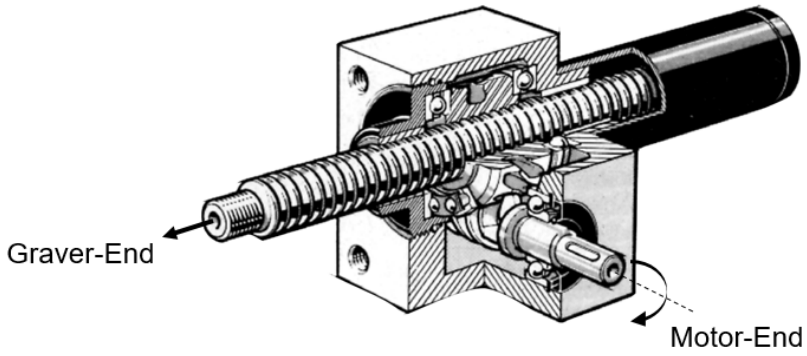

Figure 2.2.1 ANT ball screw worm gear (Adapted from ANT Antriebstechnik, 2019)

The transmission contains additional rotational and translational inertia, as well as additional damping that must be included in the graver servo model. The ball screw worm gear is also critical in the calculation and conversion of force exerted at the tool to load torque apparent at the motor. Thus, the commercially available ANT ball screw worm gear parameters were gathered to help accurately represent the graver dynamics.

The ball screw worm gear equipped in the IPF machine uses a gear ratio, N, of 6:1 to minimize the load torque applied at the motor. The efficiency of the entire mechanical transmission, η, which includes efficiency of the shafts and the gearing, is 0.55. The efficiency of the gearing alone is not documented, but most ball screw worm gear efficiencies are around 0.9. The pitch of the worm gear with rotation of the lead screw, p_{ls}, is 5 mm/rev, and the pitch of the worm gear with rotation of the motor, p_m, is 0.83 mm/rev. The idling torque of the motor, T_0, is the load torque exerted on the motor without any radial force exerted on the tool, and represents frictional effects in the motor.

2.2.1 Equivalent inertia of mechanical system

The inertia that is used in the motor model (Fig. 2.1.1) must be recalculated to encompass the inertia from the mechanical transmission and the graver translation. The inertia of the tools and lead screw must be calculated and appended to the motor inertia, J_m, to create an equivalent inertia, J_{eq}.

Energy equations were used to equate the inertia of the graver and the inertia of the lead screw separately. The kinetic energy of the graver, KE_{graver}, can be represented with a linear kinetic energy equation [2.2.1.1], simply combining mass, m_{graver}, and velocity of the tool, v_{graver}, as the tool does not rotate.

$$KE_{graver} = \frac{1}{2} m_{graver} v^2{}_{graver} \qquad [2.2.1.1]$$

The velocity of the graver can be represented as a function of pitch, p_{ls}, and rotational velocity of the lead screw, ω_{ls}:

$$v_{graver} = p_{ls}\omega_{ls} \quad [2.2.1.2]$$

The mass of the tool was approximated using the grooving tool length, l_{graver}, diameter, d_{graver}, and density, ρ_{graver}. The total inertia of the lead screw was determined using the same energy method, except that it included the linear kinetic energy related to the mass, m_{ls}, and translational velocity of the lead screw, as well as rotational kinetic energy related to the rotational inertia, J_{ls-rot}, and the rotational velocity of the lead screw:

$$KE_{ls} = \frac{1}{2}m_{ls}v_{ls}^2 + \frac{1}{2}J_{ls-rot}\omega_{ls}^2 \quad [2.2.1.3]$$

In which the mass of the lead screw was defined as a function of the lead screw dimensions, d_{ls}, and l_{ls}, and lead screw density, ρ_{ls}/l. Translational velocity of the leadscrew is equal to the translational velocity of the graver.

The rotational inertia of the lead screw, J_{ls-rot}, was calculated using its mass, m_{ls}, and diameter, d_{ls}:

$$J_{ls-rot} = \frac{1}{2}m_{ls}\frac{{d_{ls}}^2}{2} \quad [2.2.1.4]$$

The total kinetic energy of the graver [2.2.1.1] and screw [2.2.1.3] can be combined with their respective converted velocities.

$$KE_{graverandscrew} = \frac{1}{2}(m_{graver} + m_{ls})(\frac{p_{ls}}{2\pi}\omega_{ls})^2 + \frac{1}{2}(J_{ls-rot}{\omega^2}_{ls}) \quad [2.2.1.5]$$

The total inertia of these two components can then be represented as one value, $J_{graverandscrew}$, leaving out the terms $\frac{1}{2}$ and ω^2:

$$J_{graverandscrew} = (m_{graver} + m_{ls})(\frac{p_{ls}}{2\pi})^2 + J_{ls-rot}. \quad [2.2.1.6]$$

The total value of inertia was reflected back through the gearing of the ball screw worm gear to be represented at the motor. The formula for the kinetic energy of the entire system is:

$$KE_{total} = \frac{1}{2}J{\omega_m}^2 + \frac{1}{2}J_{graverandscrew}\omega_{ls}^2 \quad [2.2.1.7]$$

where ω_{ls} can be substituted with the gear ratio conversion:

$$\omega_{ls} = \omega_m / N \quad [2.2.1.8]$$

which results in a new kinetic energy equation:

$$KE = \frac{1}{2} J_m \omega_m^2 + \frac{1}{2} J_{graverandscrew} \left(\frac{\omega_m}{N}\right)^2. \quad [2.2.1.9]$$

From this new kinetic energy equation, an equivalent moment of inertia can be extracted as the inertia of the motor and the reflected inertia of the graver and screw:

$$J_{eq} = J_m + \frac{J_{graverandscrew}}{N^2}. \quad [2.2.1.10]$$

2.2.2 Equivalent viscous damping coefficient

The damping coefficient used within the motor model (Fig. 2.1.1) must also be recalculated to include the damping from the mechanical transmission. The damping coefficient of the motor, b_m, was not documented, and thus the value was estimated as 10% of the rated motor torque constant, so that at the rated speed of the motor, the damping is 10% of the rated torque of the motor.

The damping of the gear mesh was also not documented within the ANT ball screw worm gear specifications. The efficiency of the gear mesh, which would be useful in determining damping, is also not provided in documentation. So its viscous damping is estimated as the maximum for ball screw worm gears of $0.01\ N.m.s/rad$.

The damping due to the frictional contacts within the gear mesh must then be transformed through the mechanical transmission as was the inertia. Fig. 2.2.2.1 depicts the motion and interaction of the gears, simplified into spur gears for clear representation. The motor torque, T_m, is supplied at the input gear (1), which then is counteracted with torque, T_1, and damping, b_1, due to the gear mesh, as well as the inertia, J_1, of the input gear. The torque generated by the motor creates a torque on the larger gear, T_2 , which is counteracted by the inertia, J_2, of the second gear as well as the damping, b_2, and load torque, T_L.

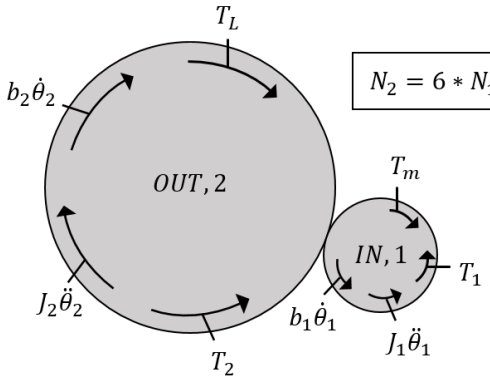

Figure 2.2.2.1 Gear mesh motion

Equations of motion of each gear were developed as follows:

$$J_1\ddot{\theta}^2{}_1 + b_1\dot{\theta}_1^2 + T_1 = T_m \quad [2.2.2.1]$$
$$J_2\ddot{\theta}^2{}_2 + b_2\dot{\theta}_2^2 + T_L = T_2 \quad [2.2.2.2]$$

And the following substitution was made using the gear ratio, N, for comparison of the two gears:

$$\frac{N_2}{N_1} = N \Rightarrow T_2 = N * T_1 \quad [2.2.2.3]$$

Another substitution was made in which rotational motion (position, speed or acceleration), can be related through the gear ratio:

$$\theta_2 = \frac{\theta_1}{N} \quad [2.2.2.4]$$

After substitution and rearrangement of equations [2.2.2.1- 2.2.2.4], the following equation of motion can be created for gear 1:

$$(J_1 + J_2(\tfrac{1}{N})^2)\ddot{\theta}_1 + (b_1 + (\tfrac{1}{N})^2 b_2)\ \dot{\theta}_1 + (\tfrac{1}{N})T_L = T_m \quad [2.2.2.5]$$

Assume that b_1 and b_2 are identical and equal to b_{gear}, as both damping coefficients represent viscous friction in the gear mesh. The damping coefficient from the mechanical transmission as seen by the motor can be associated with the rotational velocity of gear 1. The damping ratio from equation [2.2.2.5] can be combined with the damping ratio of the motor to result in an equivalent inertia, b_{eq}, to be used in the motor model.

$$b_{eq} = b_m + b_{gear}(1 + (\tfrac{1}{N})^2) \quad [2.2.2.6]$$

2.2.3 Indenting force to motor torque conversion

Using the mechanical transmission, the load torque exerted on the motor had to be calculated from the radial load force acting at the graver. The following equation [2.2.3.1] was provided by the worm gear supplier. The load torque at the lead screw, T_{L-ls}, can be calculated as a function of the load force, F_L, the lead screw pitch p_{ls}, and the total mechanical transmission efficiency, η, (Mott, 1985).

$$T_{L-ls} = \frac{F_L * p_{ls}}{2*\pi*\eta} \quad [2.2.3.1]$$

The torque at the lead screw is converted to load torque applied to the motor, T_L,using equation [2.2.2.5] and the constant idling torque, T_0, is added.

$$T_L = \frac{T_{L-ls}}{N} + T_0 \quad [2.2.3.1]$$

The calculation of the equivalent torque results in a force of 5000 N seen at the graver-end to result in approximately $1.356\ N.m$ at the motor end, which is within the rated torque of the motor, reported as $3.55\ N.m$.

Thus the following Simulink diagram could be built, now including the equivalent damping and moment of inertia of the system, as well as the load torque applied to the motor due to radial force at the indenter associated with the profile forming.

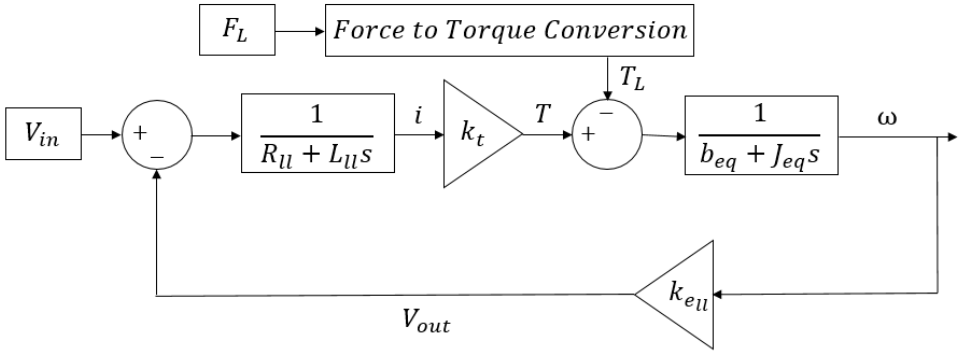

Figure 2.2.3.1 Motor model including mechanical transmission dynamics

The load force can be extrapolated from experimental data and current formulations for a given position of the graver, as mentioned in Chapter 3 and 4. Thus, a lookup table can be used for to describe the load torque from a radial force for simulation purposes.

2.3 Graver Position Servo Control

After the model of the motor was created, the control system model is required to complete the dynamics of the graver servo. Commercially available KEB controls were embedded into the IPF machine. The current form of the servo control loop was recreated, as documented by KEB, including its two feedback loops of position and velocity control to ensure accurate response and help mitigate the effects of external disturbances. Documentation indicated that the velocity loop, the inner loop, utilized Proportional-Integral (PI) control, while the position loop used Proportional (P) control. Fig 2.3.1 describes the position and velocity feedback loops of the system. However, the control system has three unknown parameters, the positional proportional gain (k_{pp}), the velocity proportional and integral gains (k_p, k_i). The desired trajectory of the graver, (θ_{in}) is an input to the servo.

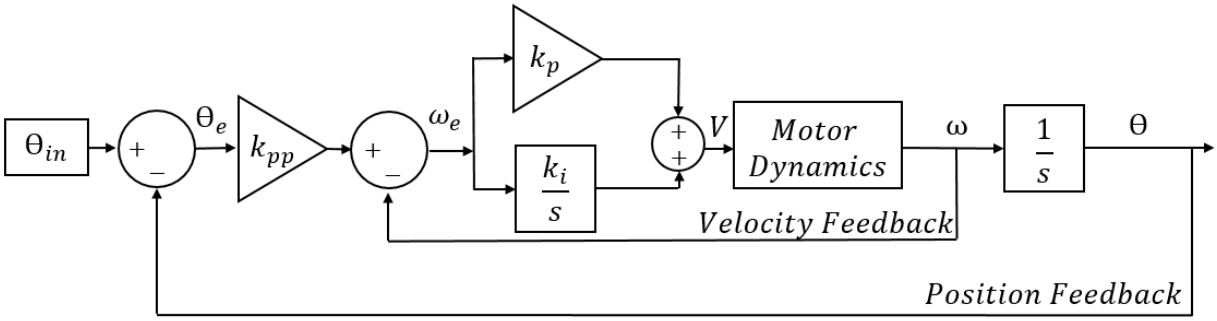

Figure 2.3.1 Position and velocity feedback control of motor motion

2.3.1 Commanded radial tool position

The input to the system, θ_{in}, is controlled by the KEB control system with a specified acceleration time of 0.1 seconds and a deceleration time of 0.2 seconds. The control logic used for the commanded position can be adapted for simulation purposes to provide a tool trajectory given a users' desired radial tool position and velocity. The control that is embedded in the model calculates the commanded trajectory of the graver given the desired final position of the graver and the nominal speed. The following piecewise function was created for positioning the graver tool in the tube material. It is determined by the given acceleration and deceleration times, the commanded position D, and velocity of the graver, both of which are values input by the user. The motion of the hydraulic feed was not studied in this research, however, and thus only radial motion is modeled from the indentation.

Table 2.3.1: Piecewise function – position(t) with $v_{graver} = 1\ mm/s$

time , t	position (t)
$0 \leq t \leq 0.2$	$-\frac{1}{2} * 5t^2$
$0.2 < t \leq D + 0.05$	$-t + 0.1$
$D + 0.05 < t \leq D + 0.15$	$\frac{1}{2} * 10 * (t - (D + 0.05))^2 - t + 0.1$
$D + 0.15 \leq t$	$-D$

The piecewise function results in a curved input. The example depicted in Fig. 2.3.1.1 demonstrates a command generated in Matlab given a desired radial tool depth of 4 mm at a feed rate of 1 mm/sec.

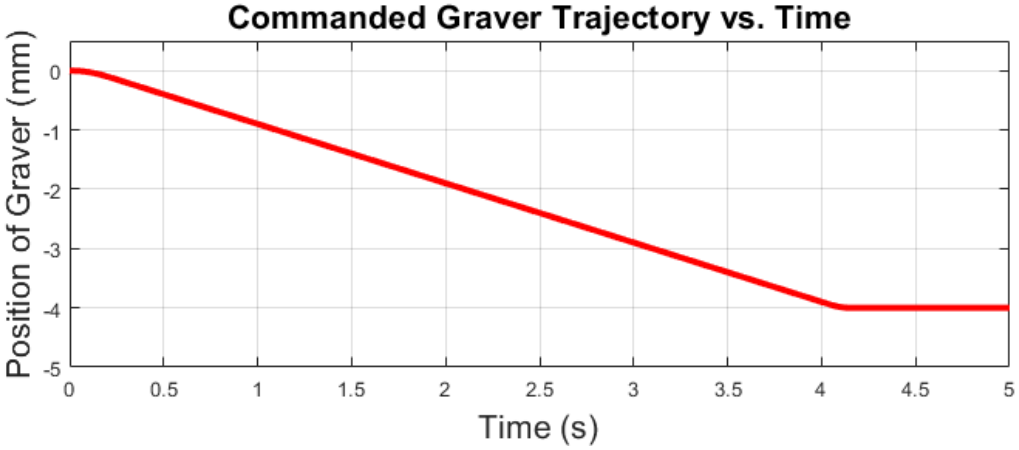

Figure 2.3.1.1 Simulation of radial graver position command

2.3.2 Design of proportional and integral gains

The gains of the graver control system provided by the KEB motor were unitless, and it was not clear if other parameters internal to the controller were not documented. Thus, the gains of the simulation were redesigned to create a model that exhibits desired control features to result in a fast and accurate response. The simulation will no longer accurately represent the actual graver controls currently installed in the machine but it is expected to represent the machine capability well. In any future experimental work, the

new controller design must be implemented into the physical machine controller if it is needed specifically, for example, for the addition of control schemes that use the graver servo here as the basis for other controllers.

The design of the controls was divided into two steps, the inner loop integral and proportional gains being designed first. An open-loop (OL) transfer function of the velocity loop was determined so that the phase margin values could be investigated to help design values for the inner-loop integral and proportional gain. The OL transfer function [2.3.2.1] was used in conjunction with Matlab's Control System Designer, and the resulting open loop transfer function determined.

$$\frac{\omega_{out}}{\omega_e}_{OL} = \frac{k_t}{LJs^2+(RJ+Lb)s+k_ek_t+Rb}\left(\frac{k_ps+k_i}{s}\right) \qquad [2.3.2.1]$$

A proportional value of $k_p = 7.2076\,V.s$ and an integral value of $k_i = 8699.57\,V$ resulted in a phase margin value of *52°*, which can be considered to be a good degree of stability of the velocity loop. The process was repeated to determine a proportional gain for the position control loop of the system, k_{pp}. The open-loop (OL) transfer function for the position loop [2.3.2.2] was also evaluated using Matlab's Control System Designer. The proportional gain k_{pp} was optimized within Control System Designer.

$$\frac{\theta_{out}}{\theta_e}_{OL} = \frac{k_tk_ps+k_tk_i}{LJs^4+(RJ+Lb)s^3+(k_ek_t+Rb+k_tk_p)s^2+k_ik_ts}(k_{pp}) \qquad [2.3.2.2]$$

A proportional value of $k_{pp} = 313\ s^{-1}$ resulted in a phase margin of *73°*. A settling time of *0.0124 s* and a peak overshoot of *2%* was achieved with this design. The bandwidth of the control system was then determined in Matlab from the closed-loop (CL) system transfer function [2.3.2.3] as 372 Hz.

$$\frac{\theta_{out}}{\theta_{in}}_{CL} = \frac{k_tk_Pk_{PP}s+k_tk_ik_{pp}}{LJs^4+(RJ+Lb)s^3+(k_ek_t+Rb+k_tk_p)s^2+(k_tk_pk_{pp}+k_ik_t)s+k_ik_tk_{pp}} \qquad [2.3.2.3]$$

The determined speed of response of the designed system and degree of stability are adequate for the IPF process to perform accurate grooving. The system response (Fig. 2.3.2.1) can be visualized using a step input to see how fast and accurate the system is. It is important to realize that the values input to the system during grooving are not step, but rather terminated ramp inputs. Hence the step response taxes the servo more than grooving inputs do.

Figure 2.3.2.1 Step response of designed control system

Finally, the entire system developed within this chapter can be simulated to exhibit the following trajectory given a commanded position of 4 mm groove depth commanded at 1 mm/s. The actual Simulink block diagrams are provided in the appendix [A1-A2].

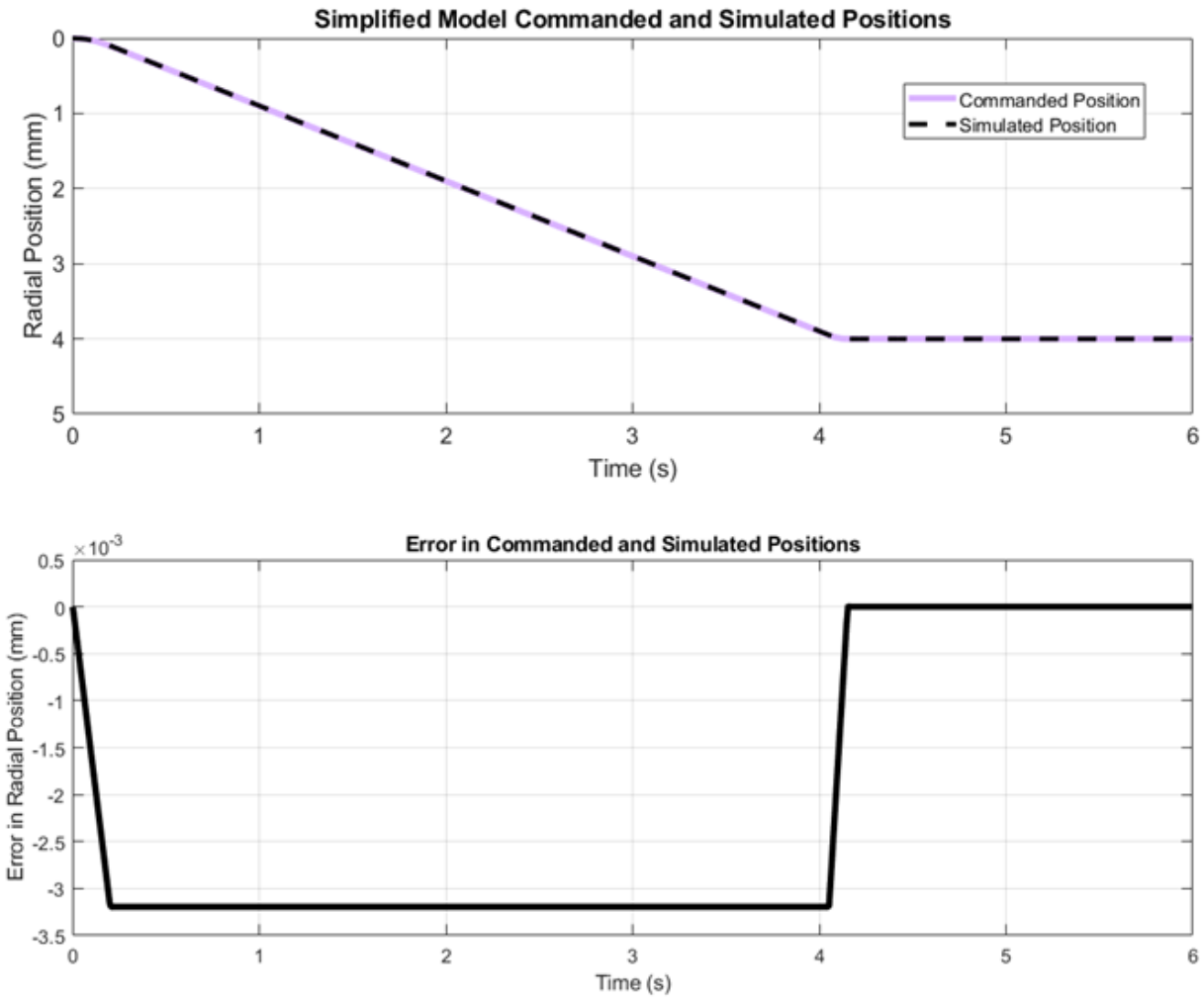

Figure 2.3.2.2 Simulation of designed control system

The above plot depicts that there is zero steady state error, and otherwise an error during indentation of $\frac{1}{k_{pp}} \rightarrow 0.00319\ mm$ since the control system is type 1. The load torque applied to the motor, and the torque required by the motor are depicted in Fig. 2.3.2.3.

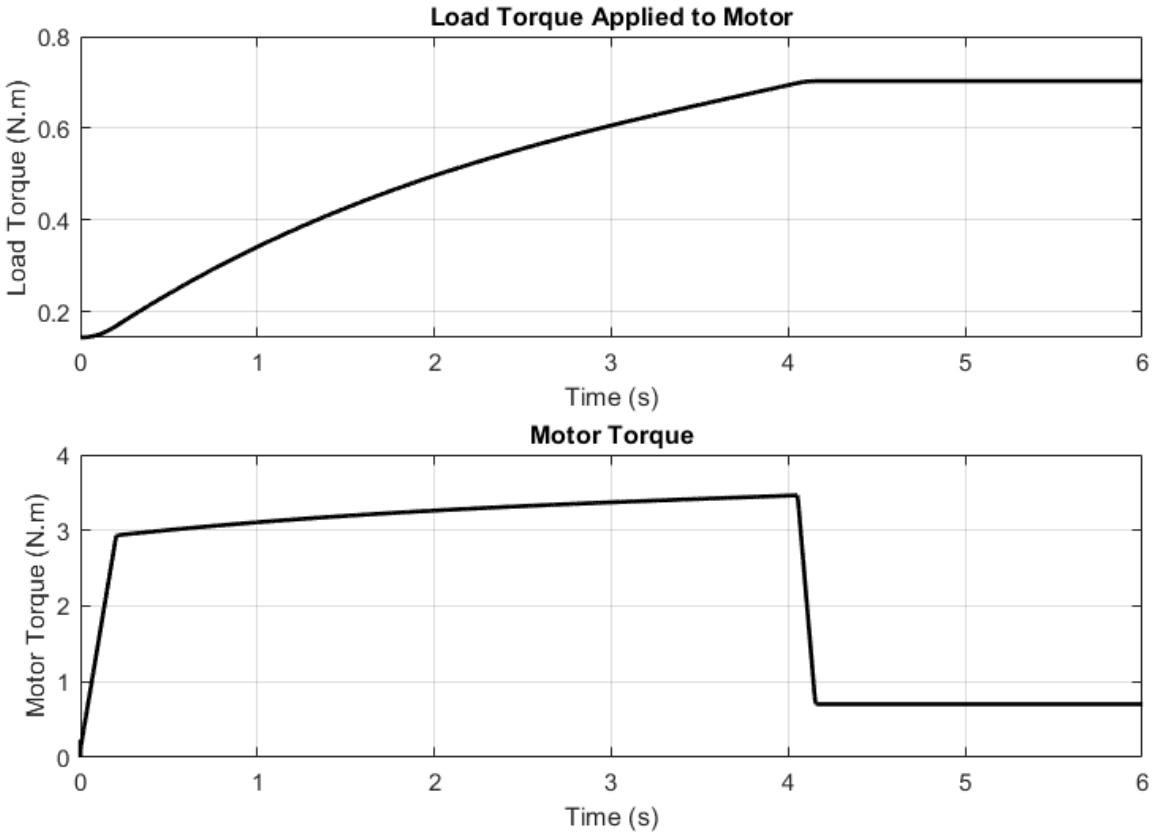

Figure 2.3.2.3 Motor torque and load torque of simulation

The torque required by the motor is reasonable as it peaks around 3.5 Nm, less than the rated motor torque.

Now that the entire KEB system has been modeled, the ideal situation would be to confirm the model and validate it with experimental data gathered from the IPF machine. However, the combination of the change in controller design here and the limitations of the experimental results in Chapter 3 prevented experimental validation of the controller. Thus, the model represented above will be assumed to be adequate for this research and for efforts involving online identification and active stiffness control described later.

2.3.3 Three phase Simulink model of BLDC motor

A three-phase model was developed in Simulink to simulate the response of the motor with greater detail. After successful modeling of the three-phase motor, the detailed motor response may be compared to the model generated in section 2.3.2. The Simulink diagram for the three phase model (Fig. 2.3.3.1 - 2.3.3.4) was created in Simulink using the specified phase to phase values for the motor, following the procedures described by Tibor, B. et al. (2011). The phase to phase values for resistance, inductance and the emf constant were used. The torque constant is not included in this simulation to compute the torque from the current. Rather, the electrical power is converted to mechanical power and then is divided by the rotational motor velocity to compute the motor torque.

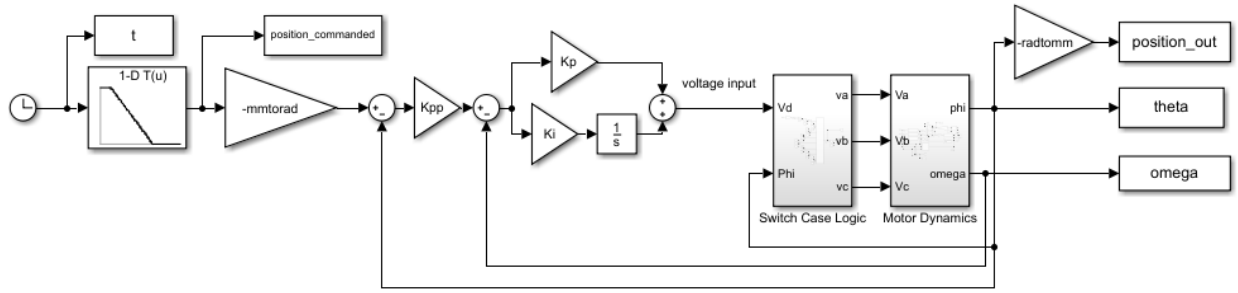

Figure 2.3.3.1 Three phase model of BLDC motor

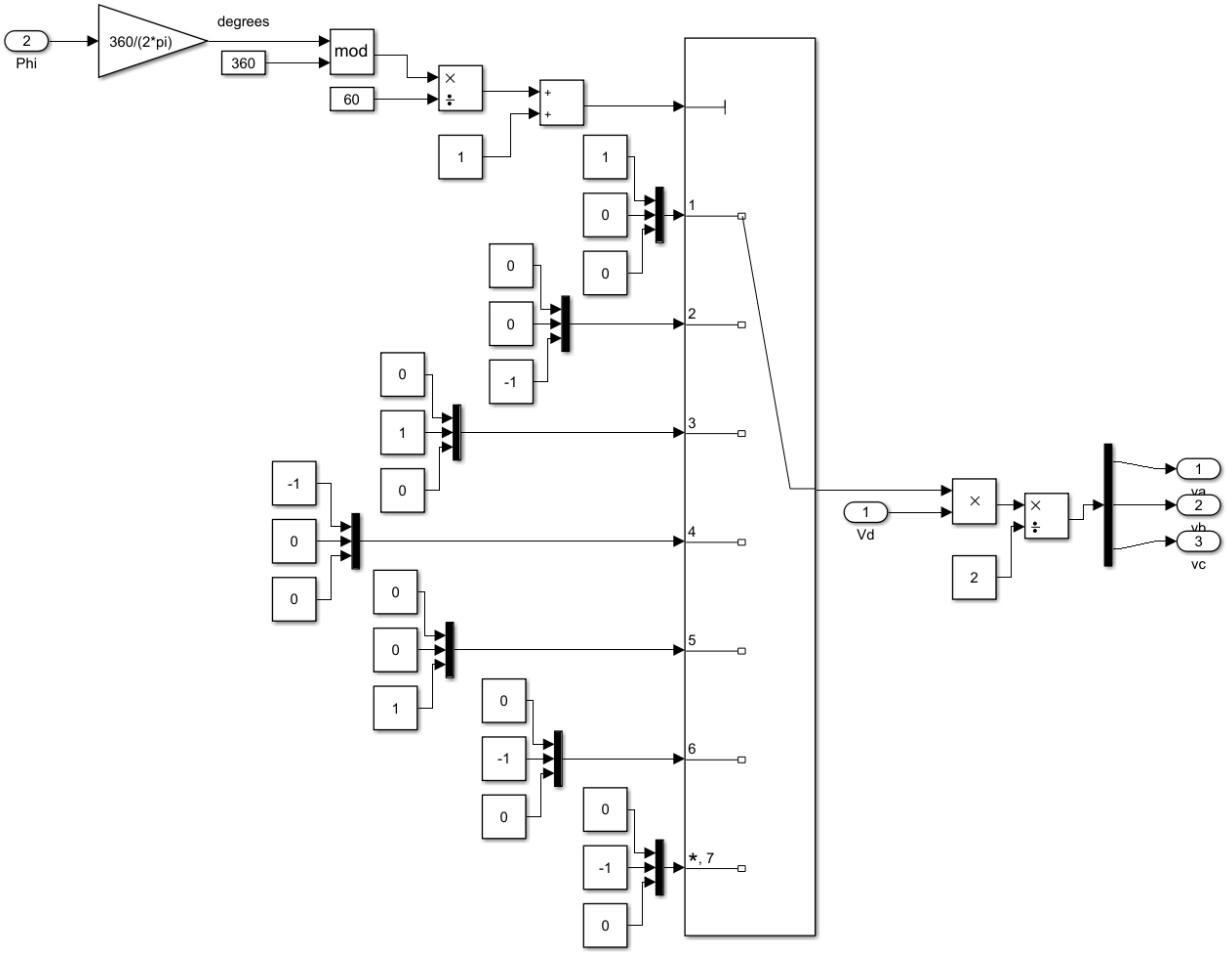

Figure 2.3.3.2 Switch case logic of three phase model of BLDC motor

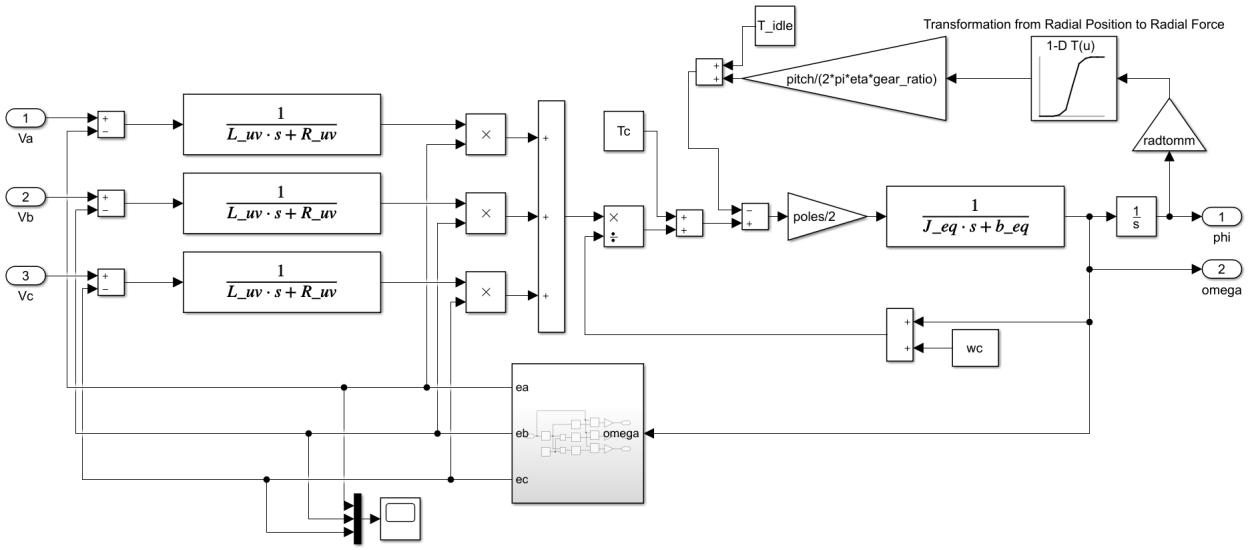

Figure 2.3.3.3 Motor dynamics of three phase model of BLDC motor

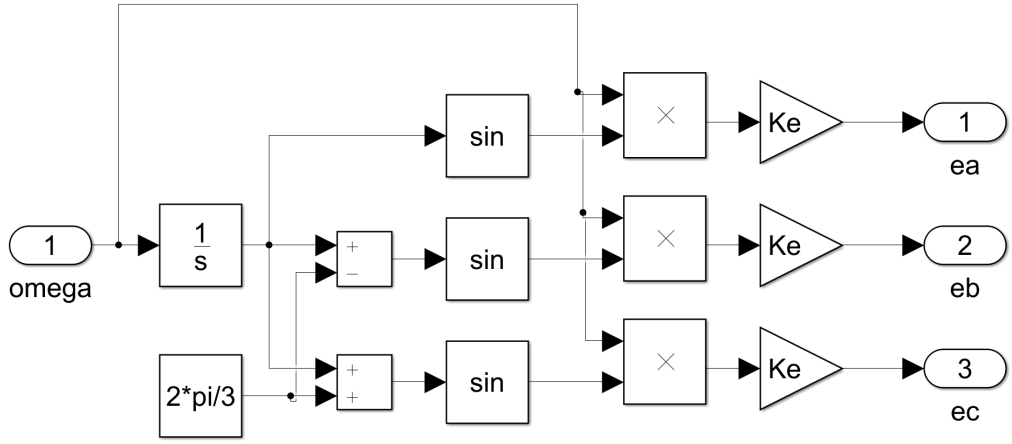

Figure 2.3.3.4 Back emf block of three phase model of BLDC motor

The three-phase model was simulated and resulted in the oscillatory response in Fig. 2.3.3.5 for a desired groove depth of 4 mm. However, the values of ω_c and T_c were unknown. To avoid the need for ω_c, the traditional torque constant equation should be used to calculate torque instead of the method mentioned above. Also, the need for T_c should be validated before the simulation can be used. To achieve a valid solution with the current Simulink set up, however, the torque value, T_c, and rotational velocity constant, ω_c, (Fig. 2.1.2.3) were adjusted to values of 3.55 N.m and 3 rad/s, respectively. These values provided the following simulations (Figs. 2.3.3.5 – 2.3.3.7)

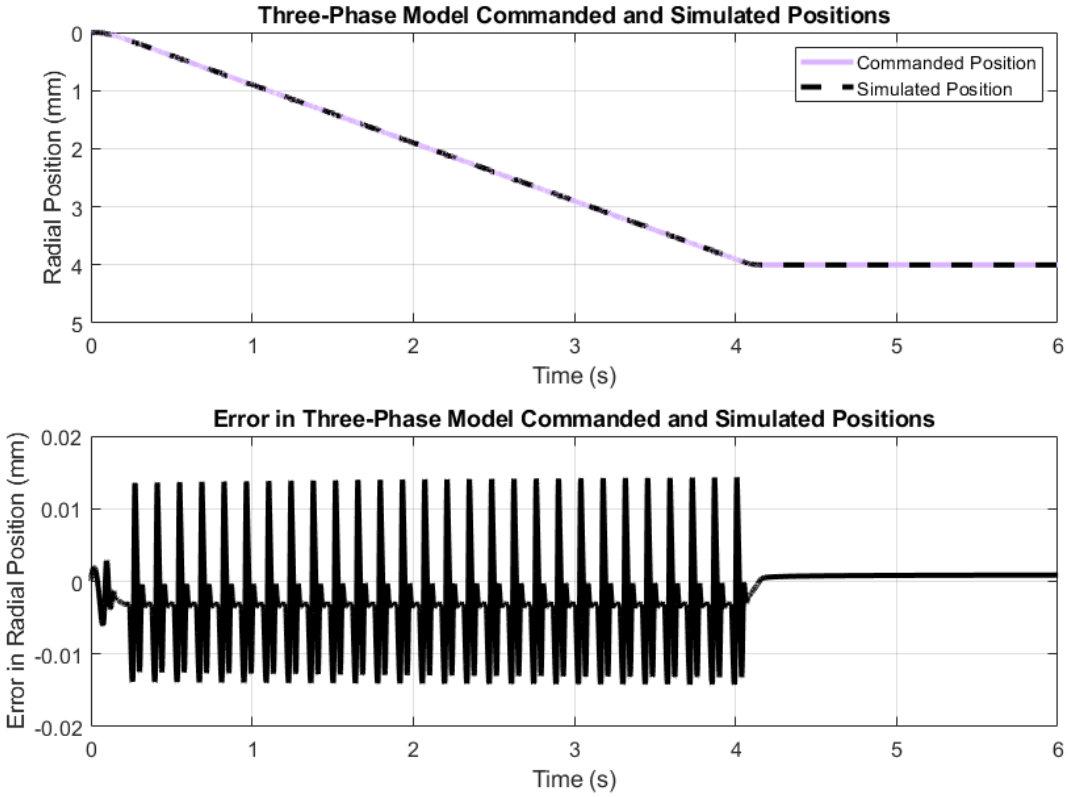

Figure 2.3.3.5 Comparison of command and simulation with three phase model

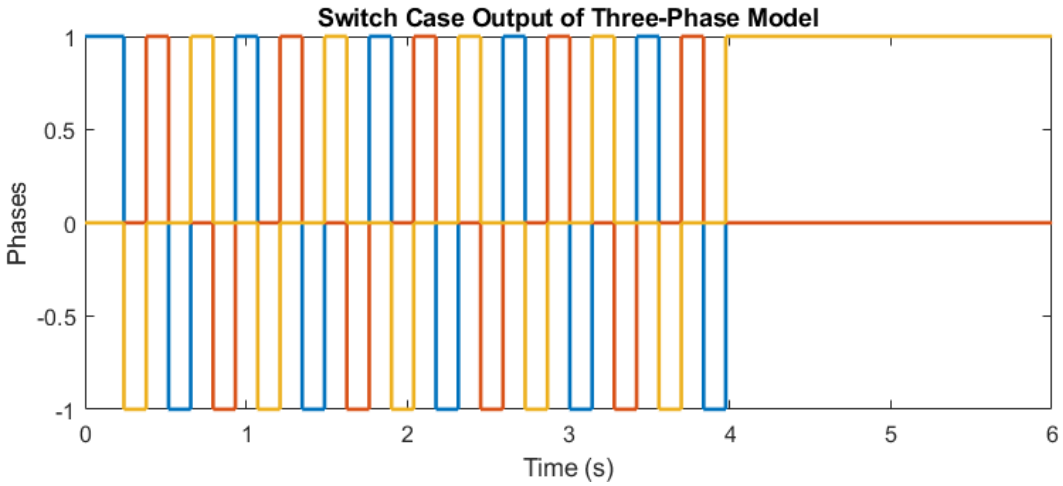

Figure 2.3.3.6 Switch case output

The back emf of the simulation was also recorded, combining the three phase voltages:

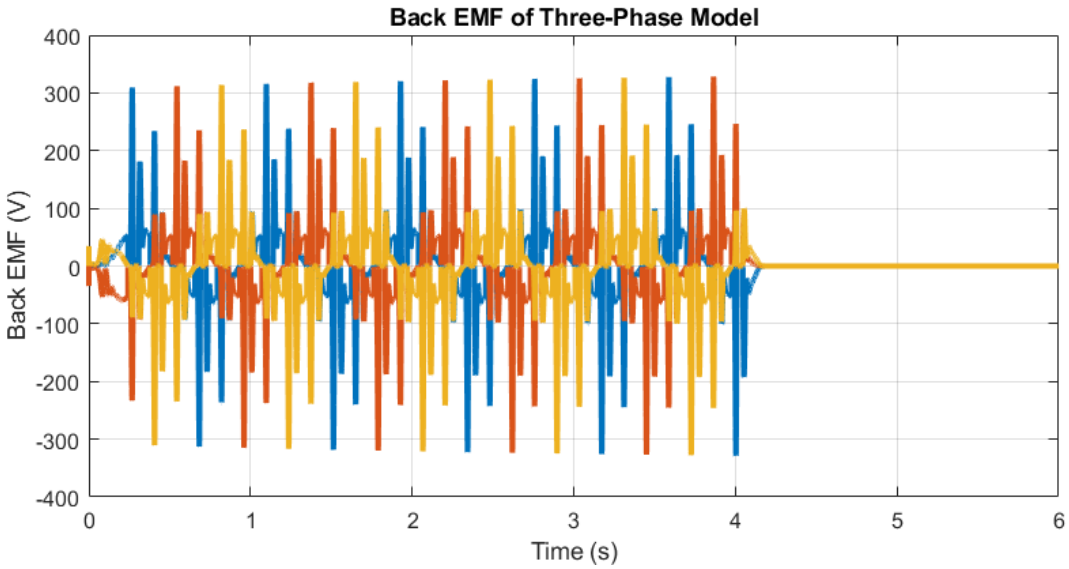

Figure 2.3.3.7 Back emf with three phase model

The values of the torque and rotational velocity change the output of back emf and change in error of command drastically. Due to the limited validation of the three phase model, a comparison is provided below of the motor velocity of both the detailed and simplified model (Fig. 2.3.3.8).To mitigate oscillations and visualize the comparison, a low pass filter of $\frac{1}{.09s+1}$ was applied to the motor velocity output from Simulink.

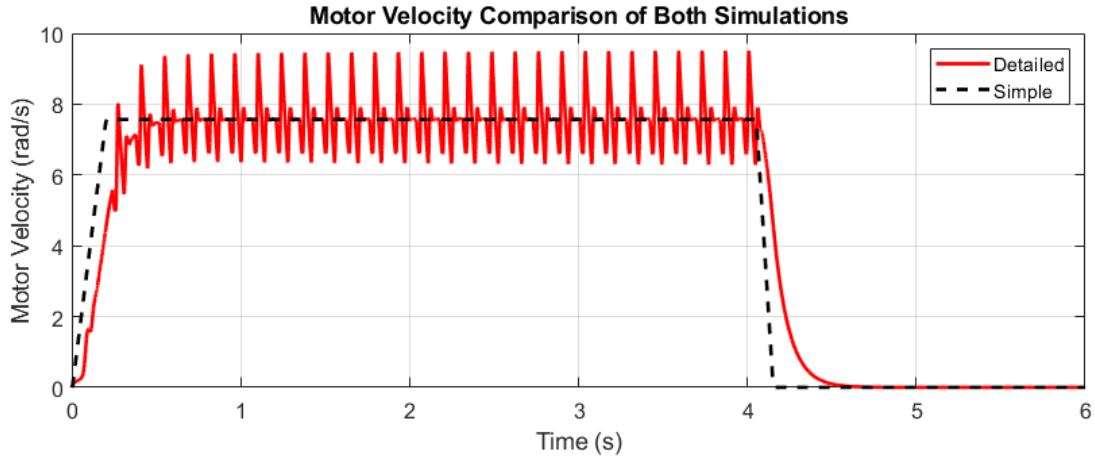

Figure 2.3.3.8 Motor velocity comparison of detailed and simplified simulations

The BLDC motor simulation needs further refinement before it can be used as a model of the IPF machine.

3 Experimental Work on the IPF Machine

The following chapter describes experimental work conducted on the IPF machine controls, along with limitations that prevented such work from validating machine control system model development. The first section describes the set up and terminology of all of the experiments. The second and third sections discuss various experiments that were conducted to provide additional insight into the IPF machine process with and without axial feed, respectively. The final section describes machine limitations and the reasons the IPF machine model could not be validated.

3.1 Experimental Setup

Experiments were conducted with similar conditions on the IPF machine within weeks of each other. Fig. 3.1.1 defines the axes of motion that will be discussed in this section, including the radial motion of the graver, and the longitudinal motion of the tube controlled by the linear hydraulic actuator.

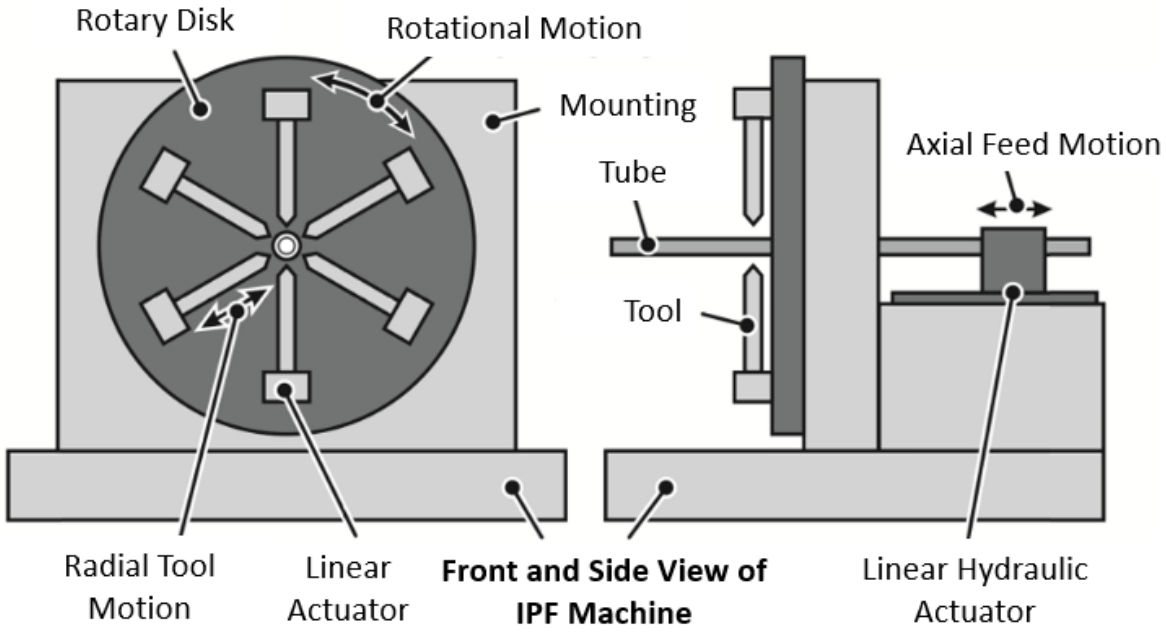

Figure 3.1.1 IPF machine kinematics (Adapted from Grzancic, 2017)

The rotational degree of freedom will not be explored in this research. Experimental parameters were held consistent throughout this research with little variation in materials and tools. A few of the variables that were held constant throughout the experimentation are tabulated in Table 3.1.

Table 3.1: Constant Experimental Parameters

Constant Parameter	Description
Tube Material	E235 Steel
Tube Thickness	1 mm
Outer Tube Diameter	40 mm
Grooving Tool	4 mm Diameter Hemispherical Graver
Support Tool	40 mm Diameter Crescent-Shaped Support
Commanded Motion about the Rotational Axis	0 Degrees of Rotation

The above parameters were chosen to reflect choices made in previously documented experiments and to promote consistency. A 4 mm diameter hemispherical grooving tool (Fig. 3.1.2 Left) was used in the following experiments. A 40 mm diameter crescent support tool (Fig. 3.1.2 Right) was also chosen for stabilization of the tube in the x-y plane to eliminate uncertainty without entirely constricting the tube.

Figure 3.1.2 Experimentation tools (Adapted from Grzancic, 2017)

Kistler piezoelectric force sensors were installed in the machine's tooling to determine the radial force that was associated with indentation (Fig. 3.1.3). The figure depicts the temporary installation of the force sensors in this machine's gravers. This installation resulted in some variability, as the graver is hand tightened around the force sensor.

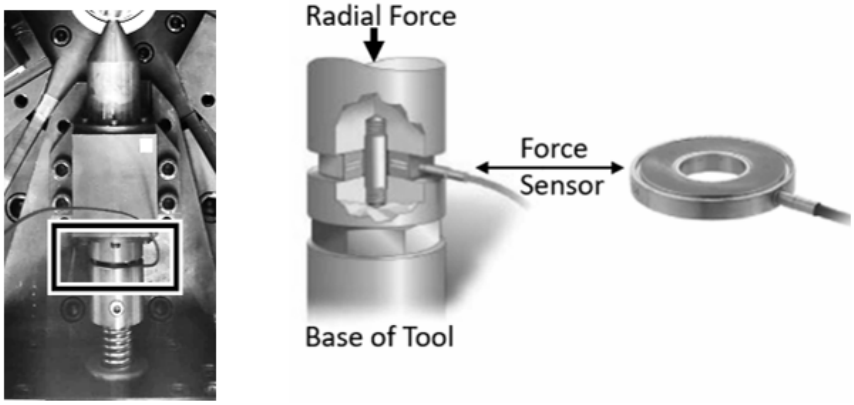

Figure 3.1.3 Temporary Installation of Force Sensor (Adapted from Kistler Group, 2009)

The force sensor collected data at 10 Hz, the same data collection rate as for the graver and feed positions. However, the data rate could be limiting the ability to monitor high frequency variations in force

measurements during grooving, and it is recommended to increase the data collection frequency rate of the system for future experimentation. After all the gravers were installed in the machine along with their force sensors, the tube selected for graving was placed in the actuator clamp of the linear actuator, and secured in place with hand-tightened bolts. Again, this method of installation results in variability in installation between experiments involving different tubes. For each experiment, the tube was lubricated with olive oil for minimal frictional effects after it was loaded into the clamp. To ensure a consistent starting position for the tools throughout all experiments, the tools were initially positioned to be roughly 0.1 mm away from touching the outer tube diameter. The 0.1 mm was measured using a sheet of paper and sliding it between the tool and the tube. Finally, the desired motions of the machine were programmed in automatic or manual mode on the HMI (Human-Machine Interface) to command a position and velocity for all eight degrees of freedom of motion. Automatic mode executes multiple lines of commands sequentially, which each include positions and velocities for all 8 degrees of motion, whereas manual mode requires one set of commands at a time for a single position and velocity of all 8 tool motions.

The unloaded contours were determined after the grooved are formed, via scans performed by the optical sensor, Micro-Epsilon ScanControl BL. The scanner was mounted on the Incremental Profile Forming machine to capture multiple tube cross-sectional profiles along the longitudinal axis. The profiles were then evaluated and compiled via Matlab to establish and create a final data set that depicted the deepest portions of the groove along the longitudinal axis. Fig. 3.1.4 depicts the setup of the unloaded contour scan.

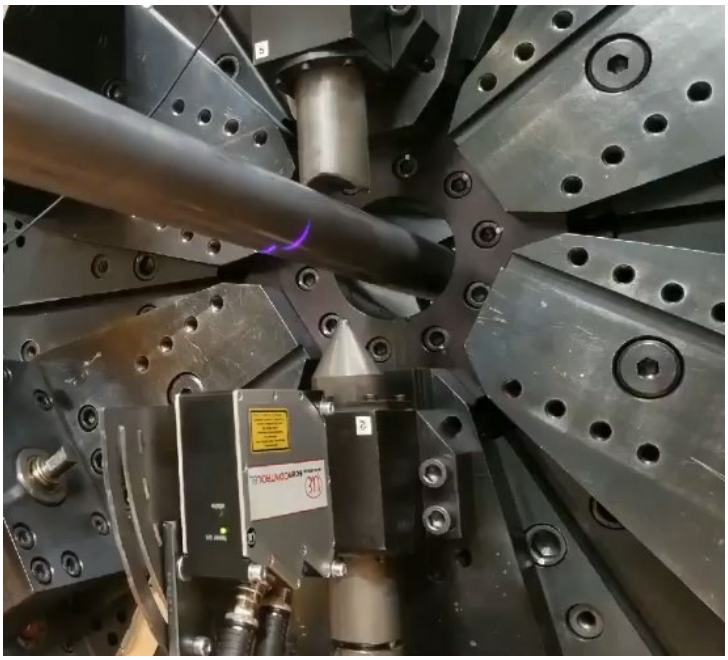

Figure 3.1.4 Micro-Epsilon scan of unloaded tube contour

The results depicted in the following section consist of positional data from the KEB encoder, force data from the Kistler force sensor, and unloaded contour data from the Micro-Epsilon Scanner.

3.2 Experiments with Axial Grooving

The following experiments depict information gathered from the IPF machine that can be useful for future experimental work. These preliminary experiments were used in setup of the other experiments discussed in this chapter, and should be taken into consideration for further experimentation on the Incremental Profile Forming Machine.

3.2.1 Determination of axial groove separation to minimize interaction

The first experiment conducted was to determine the distance necessary between grooves to isolate the structural response of the tube during the forming experiments, that is, to ensure that the process response was not affected by the presence of an adjacent groove. For this experiment, three different depths of 50 mm long grooves were created, flanked on both sides by 300 mm long sections of ungrooved tube. The contour data was gathered after the grooves had been created, along with force data during grooving. The following three plots help determine the groove spacing needed to ensure that the presence of adjacent grooves does not impact experimental results. The following plot shows the 2 mm, 4 mm, and 6 mm grooves created.

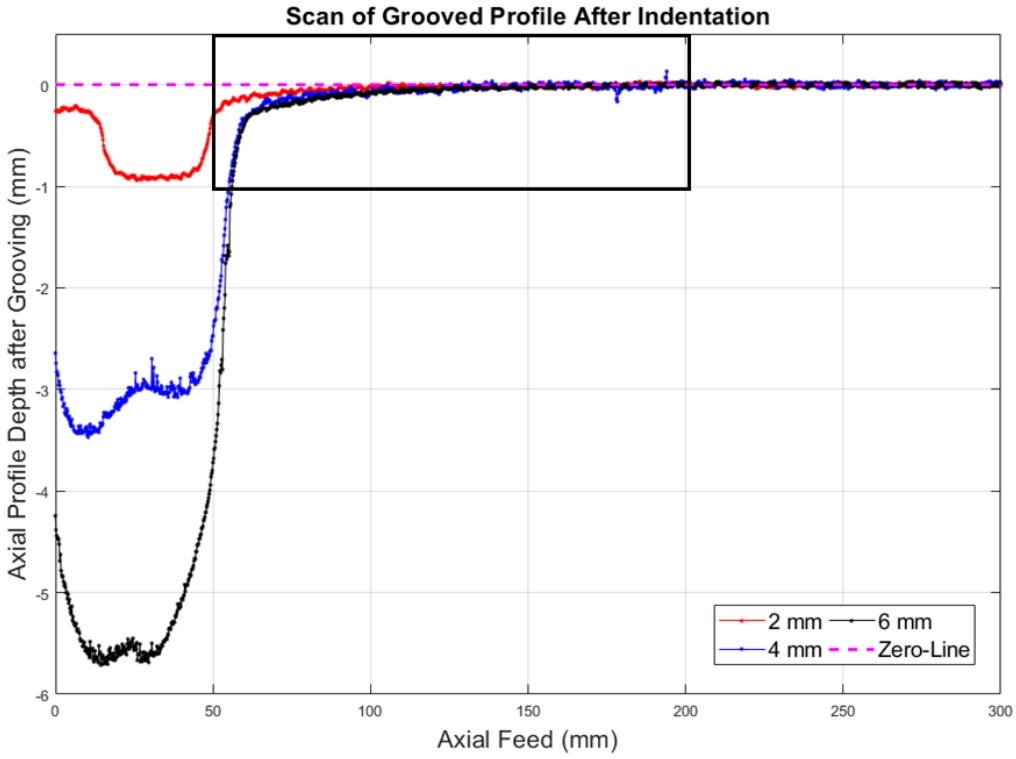

Figure 3.2.1.1 Scan of the unloaded grooved profile

Fig. 3.2.1.2 shows the data contained within the black rectangle within Fig. 3.2.1.1.

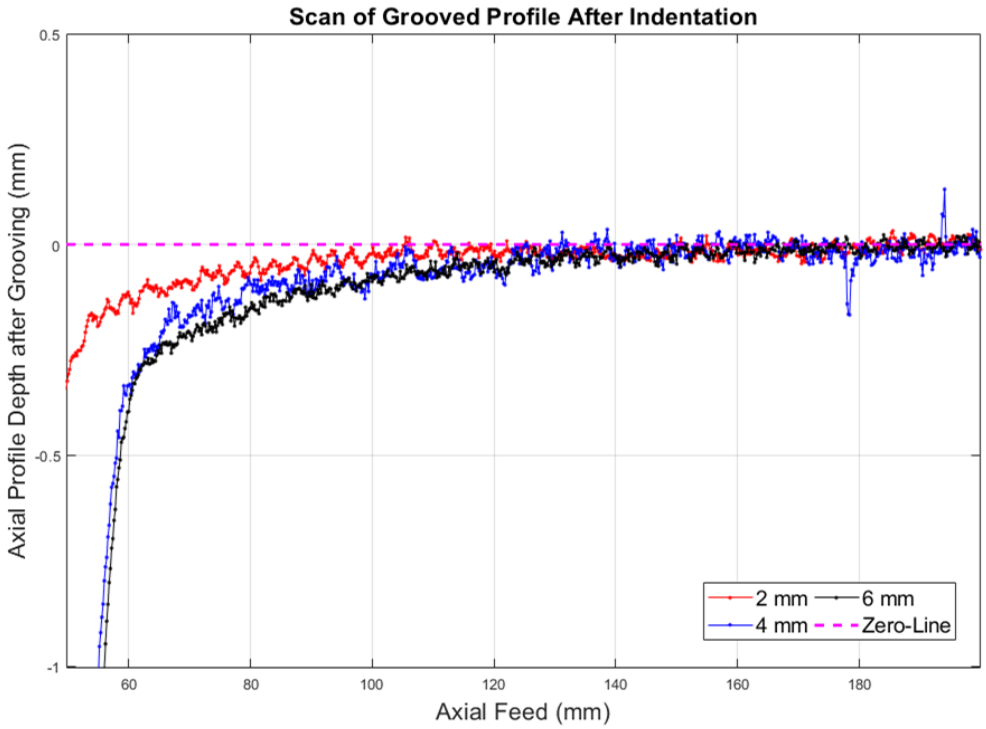

Figure 3.2.1.2 Zoomed-In scan of the unloaded grooved profile

The results in Fig. 3.2.1.1 and Fig. 3.2.1.2 depict the distance necessary to allow the tube to return to its original undeformed condition following a groove. Tube deformation returns to the zero position around 120-140 mm from the beginning of the groove, indicating that approximately 70 to 90 mm of gap spacing, on each side of the groove is needed, following and preceding the 50 mm long groove. This data was used in the following experiments to ensure the effect of adjacent grooving was mitigated.

3.2.2 Effect of tool path trajectory on unloaded groove geometry in axial grooving

Another experiment was performed to determine the effects of the angle of entry of the grooving tool into the tube material. Prior experimentation by Grzancic (2017) indicated that radial indentation followed by axial grooving resulted in significant groove depth errors, and thus the effect of tool trajectory on the groove depth must be identified for further material deformation analysis. The following experiment created a 500 mm long groove with tool trajectory angles at entry and exit being 21.8, 45 and 90 degrees. The trajectories of the grooving tool are shown in Fig. 3.2.2.1.

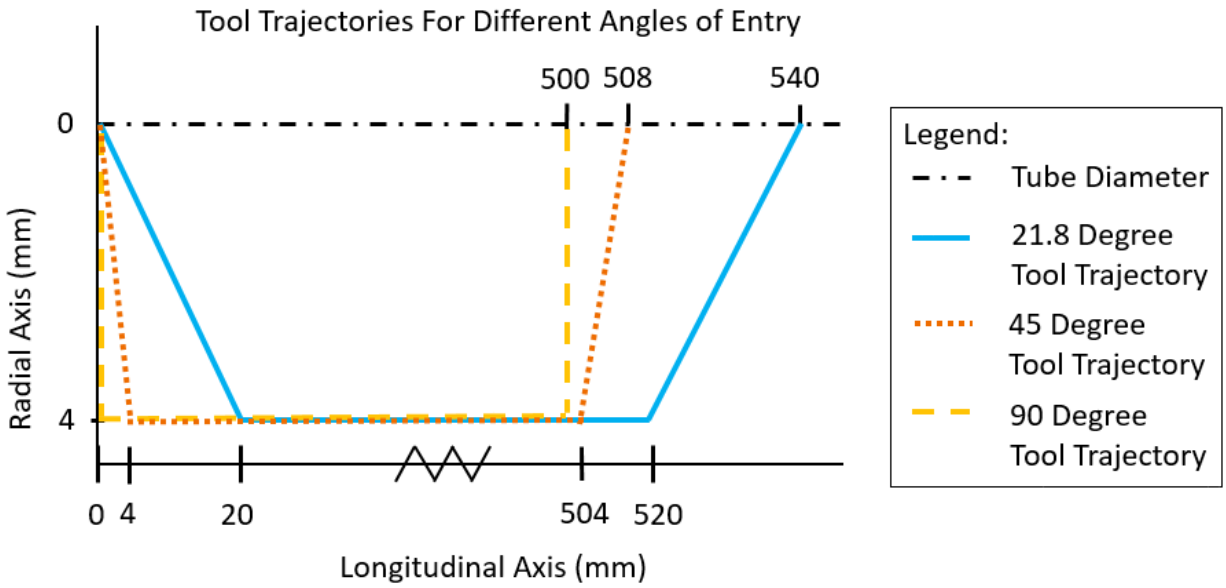

Figure 3.2.2.1 Tool path trajectories for various commands

The variation in angle could only be manipulated through variation of either graver or feed speed. Thus, the graver velocity was constant at 2 mm/s while the hydraulic feed speed changed from 0 to 2 to 5 mm/s during graving, resulting in the various angles depicted in Fig. 3.2.2.1.

The contour data of this experiment was then gathered using the MicroEpsilon scanner as described in section 3.1, and resulted in the unloaded contours along the longitudinal axis depicted in Fig. 3.2.2.2. The following plot depicts the raw data that was collected with the optical sensor.

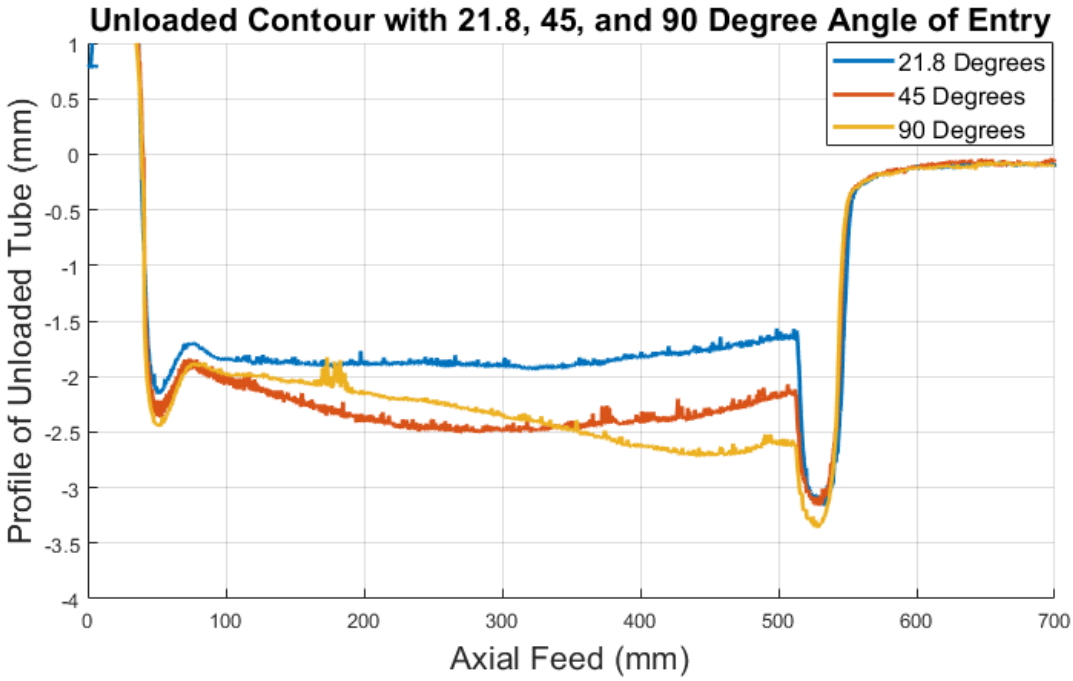

Figure 3.2.2.2 Unloaded contour of tool trajectories with various angles

The plot above depicts that the 21.8 degree angle of trajectory entry creates the smallest deviation at the center of the groove. The 90 degree entry deviates greatly from its intended constant depth, whereas the 21.8 and 45 degree angles of entry greatly improve the accuracy of the contour. Thus, the smallest angle should be used to mitigate effects of tool path entry of the graver on the groove geometry.

3.2.3 Radial indenting force – groove depth relationship

Force measurements were collected in another experiment to identify a relationship between graver position and force on graver. The intention of this experiment was to determine the forming force during grooving that may then be utilized in the model of the graver servo dynamics. The relationship between force and position was then directly implemented into a 1-D lookup table in Matlab. Therefore, a given position registers a certain external force, which then can be transformed into a load torque as was described in Chapter 2.

An axial feed speed and graver speed of 1 mm/s were utilized, corresponding to a 45 degree descent of the tool trajectory with respect to the longitudinal tube axis. Three different runs were executed with final groove depths of 2 mm, 4 mm, and 6 mm. Fig. 3.2.3.1 depicts the force of the graver corresponding to graver position at that time.

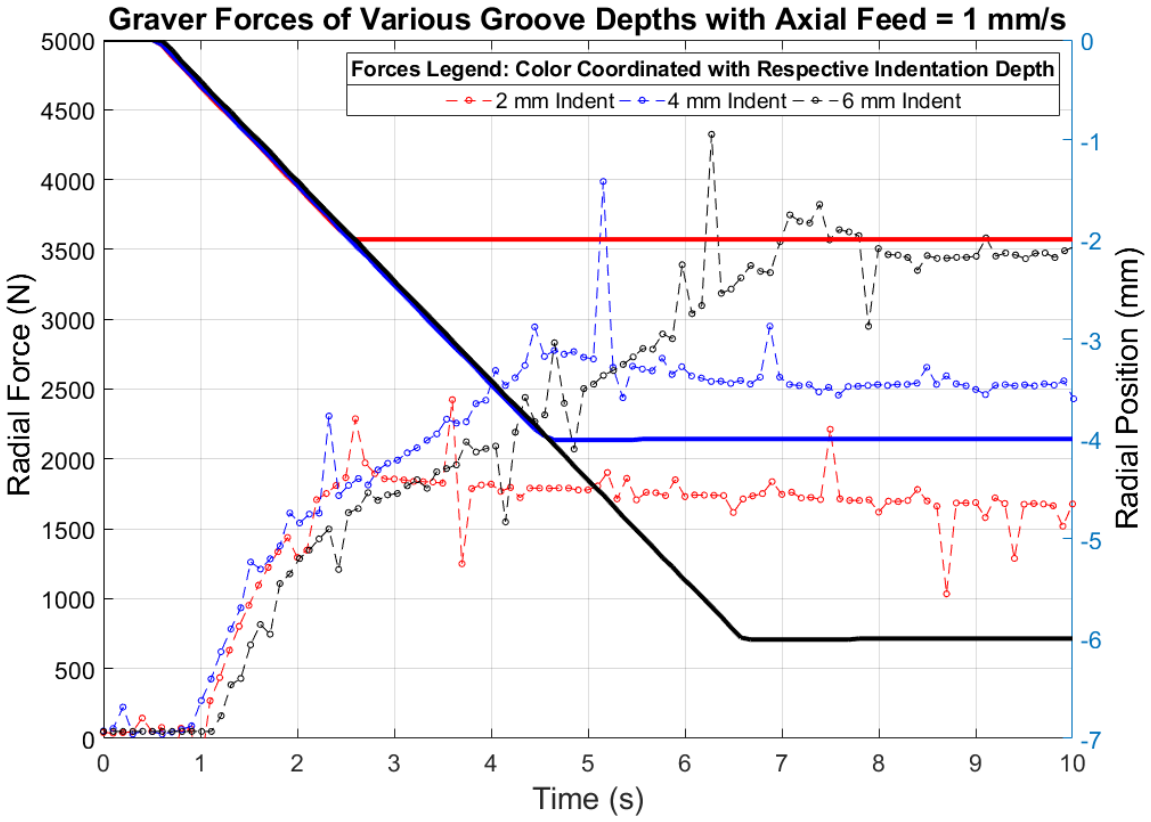

Figure 3.2.3.1 Radial force versus position for various groove depths

Figure 3.2.3.1 demonstrates the consistency between the forces given a certain radial position of the grooving tool upon entry. Due to the similar trends of measured forces for all three depths, a single 1-D lookup table is used for any depth input into the model using the force and position data from the 6 mm

groove. The following figure depicts the force that will be modeled acting at the grooving tool given its respective radial position.

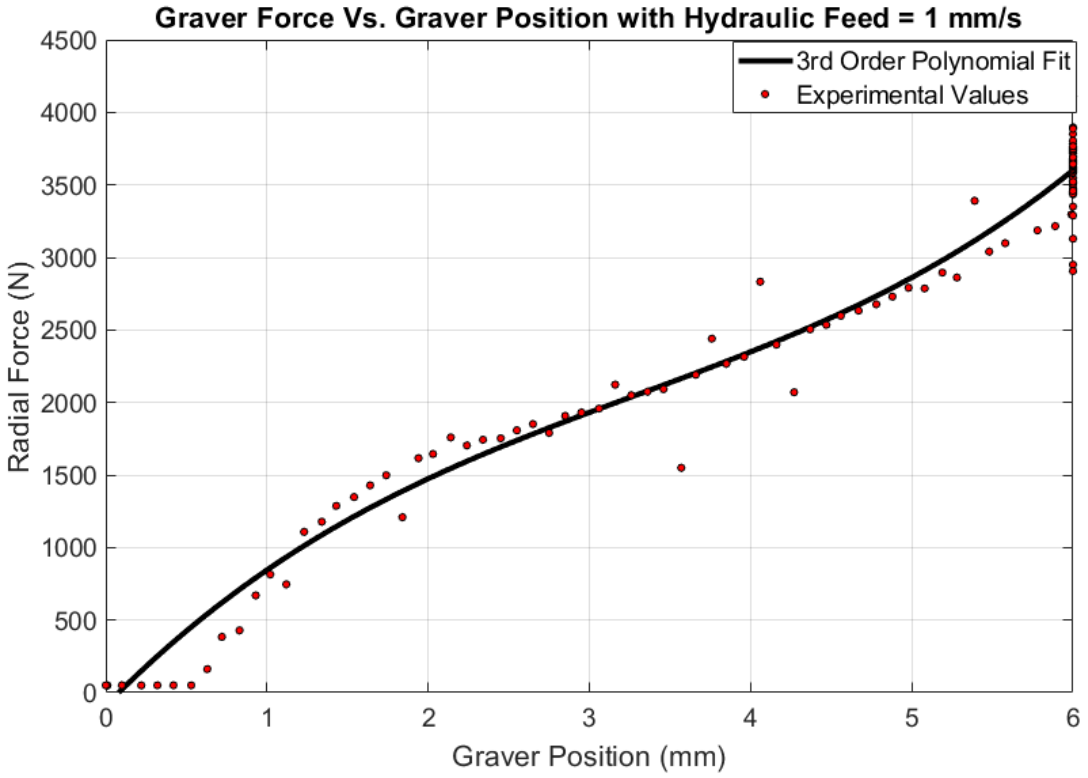

Figure 3.2.3.2 Radial force versus position used in lookup table

The relationship between force and position of the tool was modeled using a least-squares 3rd order polynomial fit, as it seemed to capture the experimental data the best. However, the physics of the grooving process has not been modeled, and thus the accuracy of this polynomial fit does not capture the true mechanics behind the forming force developed due to radial grooving. Further, current simulations are only valid for the radial motion of the graving tools, as the model of a hydraulic feed has not been simulated yet. Thus, a force and position relationship without axial feed should be created and compared to represent accurate radial forces that would develop within the current scope of dynamics modeled in the graver simulation. Such experiments have been conducted and recorded by Grzancic (2017), and were also conducted and recorded in 3.3.2.

3.2.4 Radial indenting force – groove depth relationship for small radial increments

Next, experimentation was conducted to determine the effect of a minimal increase in indentation about a constant groove depth. A trajectory of 21.8 degree angles of entry with respect to the tube axis was utilized for the increment. A groove length of 500 mm was used to further mitigate these end-condition effects. The constant groove depth was 4 mm, and the increase in depth was executed halfway along the groove with increments of 0.0, 0.1, 0.2, and 0.3 mm.

The contours were gathered after processing with the Micro Epsilon Scanner. The point at initial indentation should have remained similar throughout all of the experiments, as the commanded grooves

were identical until the radial position of the graver was incrementally increased after an additional 250 mm along the longitudinal axis. Therefore, in the following contour plot, the initial indentation point at 0 mm along the longitudinal axis were aligned.

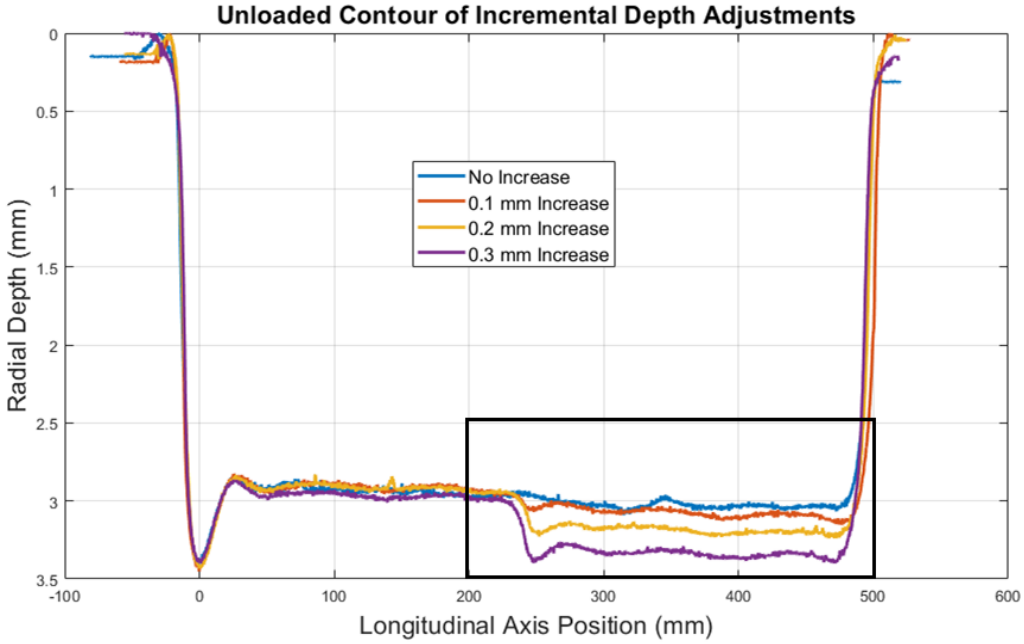

Figure 3.2.4.1 Unloaded contours following minimal incremental changes in groove depth

Figure 3.2.4.2 represents the data within the black box pictured in Figure 3.2.4.1.

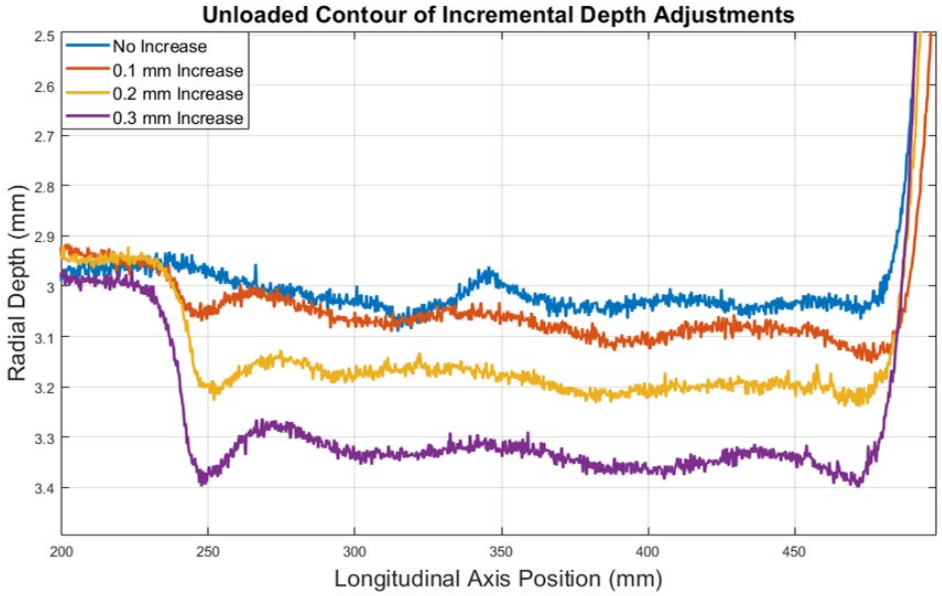

Figure 3.2.4.1 Zoomed-in unloaded contours for minimal incremental changes in groove depth

While the scanned contour depths follow a trend of increasing with increasing increments, as expected, the variation in measured depth before the incremental change in groove depth is too large in comparison to the depth of the contours measured after the increment in depth. Therefore, the contours after the additional indentation cannot be compared for linearity.

The force data was also gathered from this experiment and was expected to have a positive correlation with increase in incremental groove depth. However, the following tabulated force results were obtained, that limit the viability of using this data to create a relationship between force and an incremental change in graver position.

Table 3.2.4: Force vs. Increase in Indentation

Additional Indentation of Graver (mm)	Difference in Average **Graver** Force Before and After Indentation (N)	Difference in Average **Support Tool** Force Before and After Indentation (N)	Difference in Average **Graver and Support Tool** Force Before and After Indentation (N)
0.0	-34	-10	-44
0.1	276	-5	271
0.2	176	17	193
0.3	270	12	282

The forces do not incrementally increase as the additional indentation does, either for the graver forces, the support forces, or a combination of both the graver and support forces. The relationship between force and unloaded contour cannot be further investigated using this experiment, as planned.

3.2.5 Radial indentation force measurements for different tool trajectories

The following experiment was conducted to contrast the difference between indentation with and without hydraulic feed. A 50 mm long groove of 4 mm in depth was created in the following experiment, and was repeated four times for consistency. Immediate indentation refers to no axial motion during the radial indentation speed of 1 mm/s, while gradual indentation refers to a speed of 1 mm/s for both the radial and axial motions, creating a 45 degree angle of the tool trajectory during indentation.

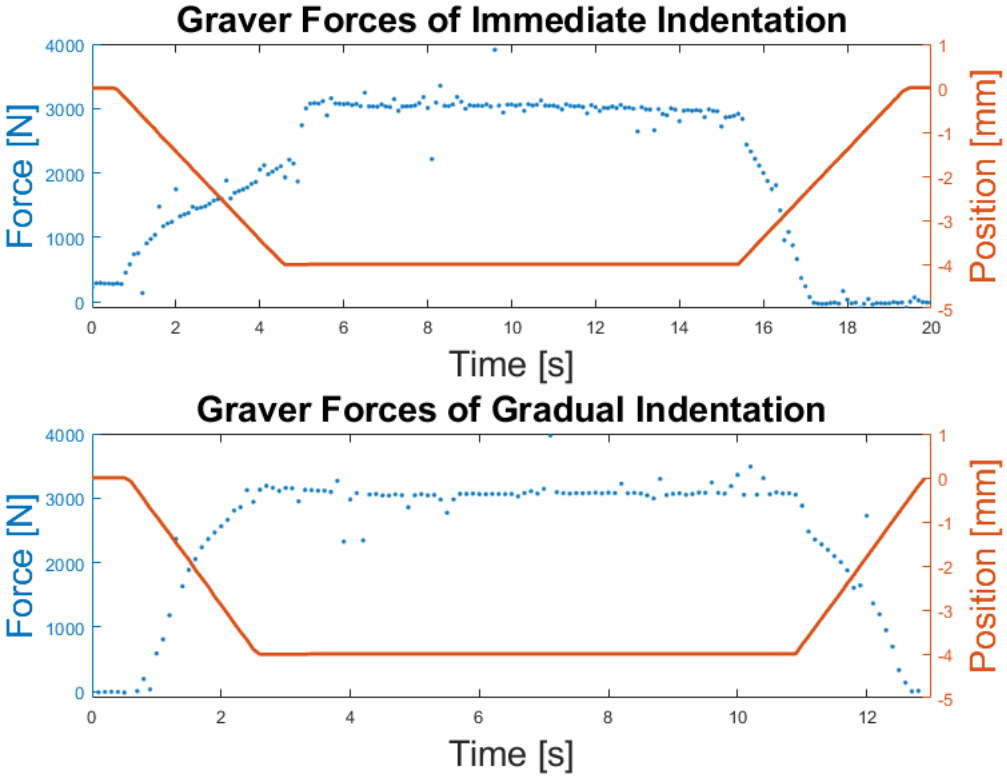

Figure 3.2.5.1 Immediate and gradual radial forces and position of grooving tool

The force pattern depicted above (Fig. 3.12) was confirmed after four iterations of the same experiment. The data above depicts that an additional 1000 N is exerted on the force sensor during the longitudinal grooving of the tube. This implies that during axial grooving, an additional 1000 N is applied to the force sensor. These results contradict previous results obtained by Grzancic (2017), and are further explored in 3.4.5.

3.3 Experiments without Axial Grooving

Radial indentation experiments were conducted, and more information was gathered. These experiments were compared to those conducted with axial feed.

3.3.1 Unloaded contours for various groove depths

The following experiment considered 5 depths: 6, 6.1, 6.1, 6.2, and 6.3 mm of radial indentation depth without any axial motion. The radial indentation speed was set to 1 mm/s. The goal of this experiment was to investigate the difference in the unloaded contours and forces for small changes about a certain depth, 6 mm. Fig. 3.3.1.1 depicts the unloaded groove contours after indentation. The contours were aligned with their left most point at a radial zero-position, and the deepest scanned position of the groove was labeled as the longitudinal axis zero-position.

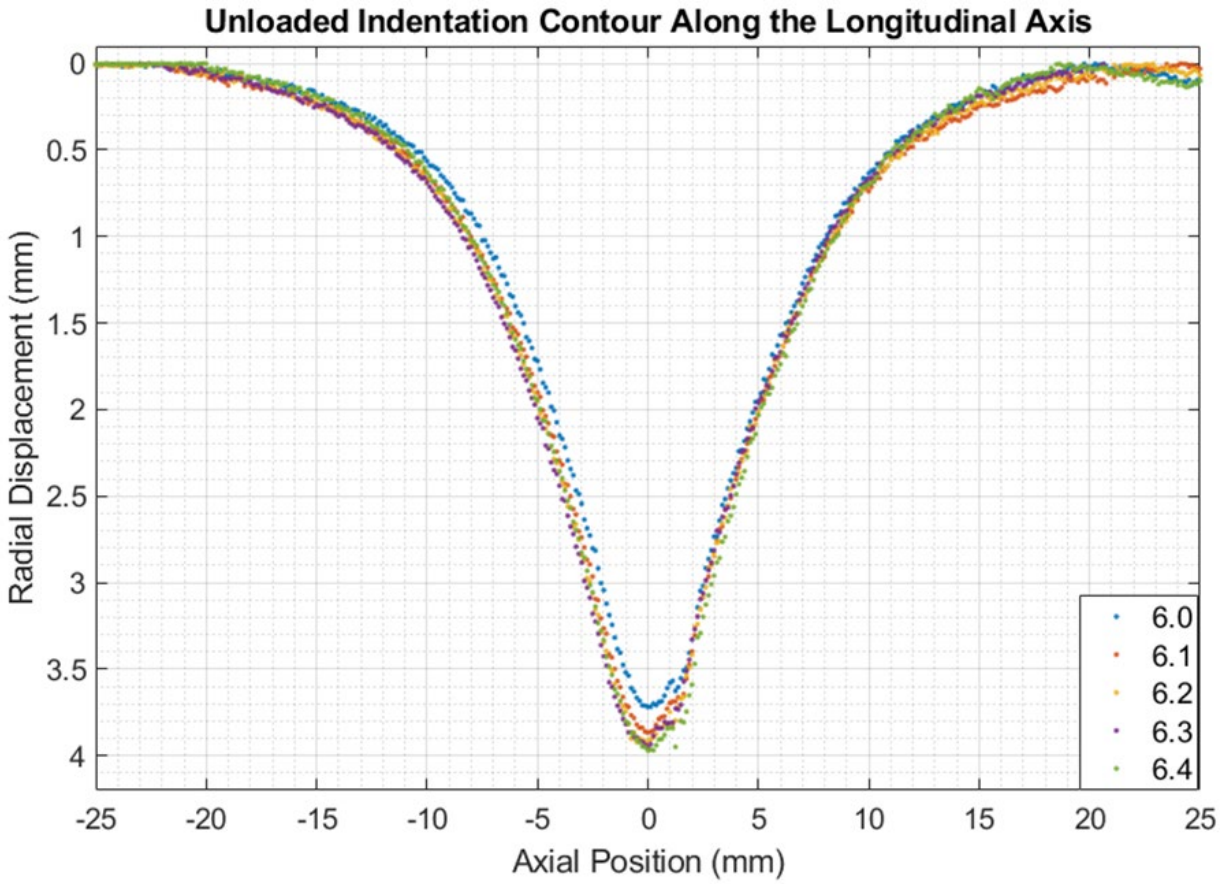

Figure 3.3.1.1 Unloaded contours for various indentation depths

Figure 3.3.1.1 captures the consistent increase in depths scanned after work piece is grooved and unloaded.

3.3.2 Unloaded contours at various groove depths

The following experiment created three groove depths at with no axial feed during indentation. These plots can be compared to those that were developed in section 3.2.3 with axial feed. The elimination of the axial feed may result in a more accurate force lookup table to be used with the current model of the indentation servo dynamics.

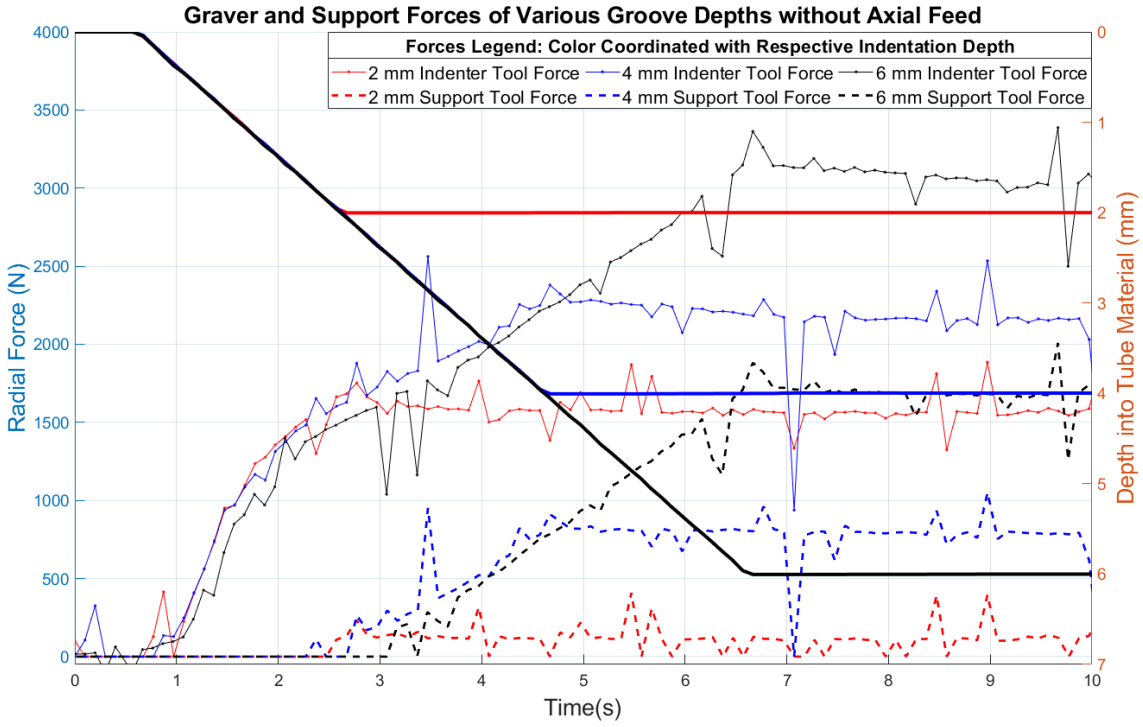

Figure 3.3.2.1 Grooving and support tool forces without axial feed

Fig. 3.3.2.1 was created to show how the forces are distributed between the grooving and support tools. The data pictured shows how the indenting force is distributed between the graver and the support tool. The force data collected could also be compared to force data collected during axial grooving as described earlier.

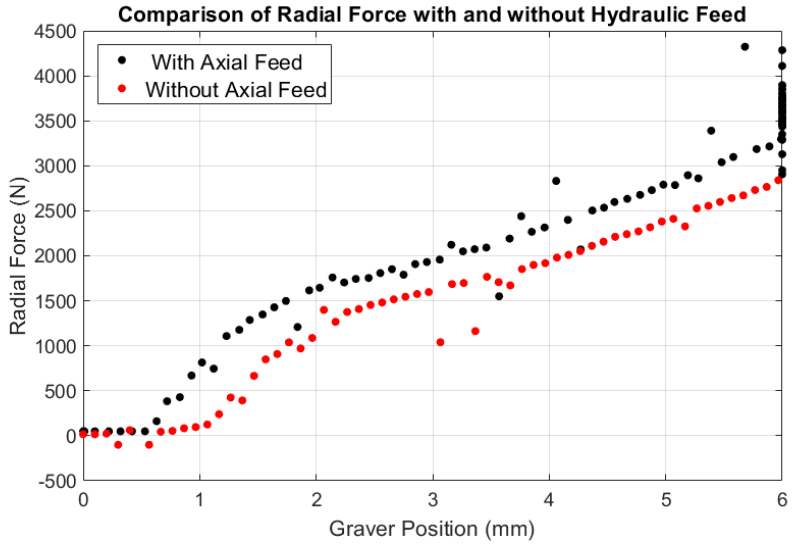

Figure 3.3.2.2 Comparison of radial force with and without axial feed

The force with axial feeding is greater than without. There is variation between the radial force and radial position relationship depending upon if there is axial motion. Further experimentation should be done to validate the reason for this larger reading of force developed with the axial feed.

3.4 IPF Machine and Process Limitations

During experimentation, machine and process limitations were identified. The following sections capture observations and analyses that were made based on experiments, including those described within Section 3.2, which depicted incomplete results due to machine limitations. Sections 3.3.1 and 3.3.2 provided reasons why the Incremental Profile Forming machine dynamics models cannot be validated with experimental results conducted during this research.

3.4.1 Timing limitations with initiation of command for graver servo

In the following experiment, an indentation of 4 mm was commanded to the machine graver independent of any other tool motions. The resultant positions recorded by the encoder during the process are plotted against time in Fig. 3.4.1.1.

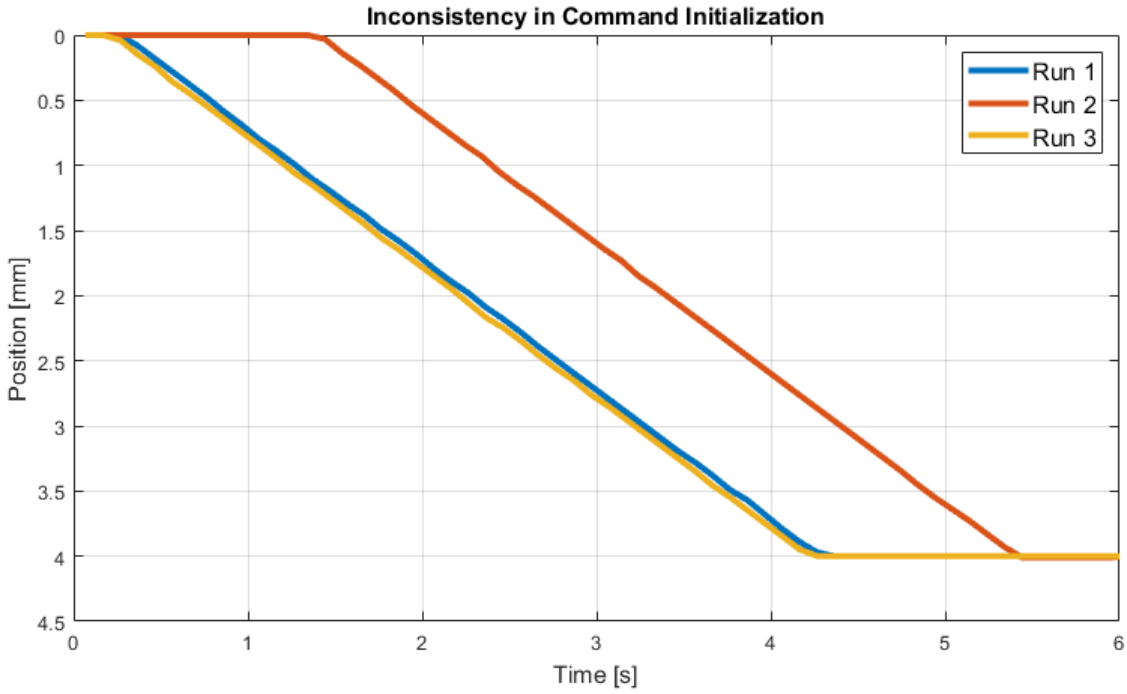

Figure 3.4.1.1 Commencement of graver radial position

All of the recorded positions above should ideally align with one another along the time axis, as the same command was programmed in the HMI for all three runs. Fig. 3.4.1.1 shows that the initially recorded time varies between the three runs. To account for the time needed for the first recorded command, the data was also plotted adjusting all the initial times to begin at zero seconds along the time axis. The following plots were obtained after setting all of the initial values of the recorded tabulated position data from the IPF machine to zero:

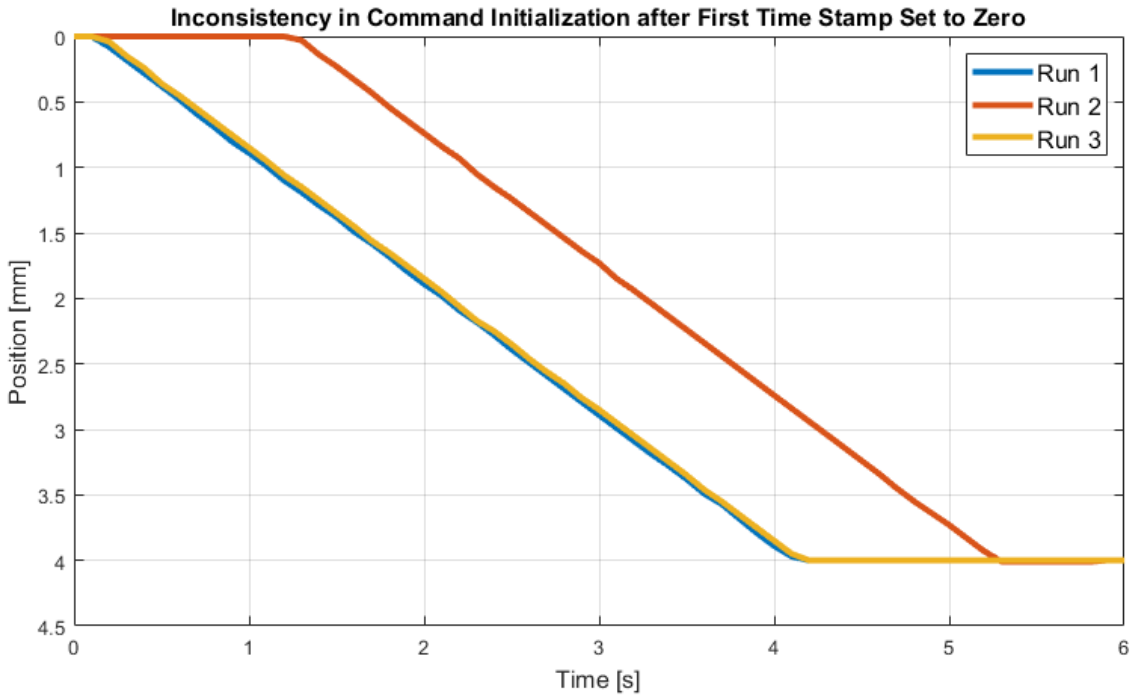

Figure 3.4.1.2 Commencement of graver radial position after initial time alignment

Even if the initial time is aligned as in Fig. 3.4.1.2, the position does not line up along the horizontal time axis as it should, given the same command for all three runs. The control method the machine utilizes to initialize itself is not repeatable. Upon initialization of the command, the values observed on the HMI oscillate as they attempted to replicate the values set as the 'initial positions' of the process. The process would not commence until these values corresponded to the set initial position of the commanded positions of all 8 degrees of motion. Occasionally, the hydraulic feed position did not and could not match its initial commanded value, and thus, the system would need to be reset and the command would need to be programmed once again into the HMI. For these reasons, it is not clear when the command is sent to the graver, as depicted in Figure 3.4.1.2.

Another consideration for the misalignment in Fig. 3.4.1.1 was to evaluate the times when the hydraulic feed lines up with the initial commanded hydraulic feed position to determine when the command commences. However, the hydraulic feed position is recorded to the nearest millimeter in automatic mode. The machine is capable of recording a feed position with precision of hundredths of millimeters, but during commencement of the command, the precision is eliminated, hindering an investigation of hydraulic feed alignment.

3.4.2 Settling time limitation of graver servo dynamics

Tabulated data from experiments in section 3.3.1 hinders validation of the model developed within Chapter 2. The settling times for the 5 experimental runs are tabulated in Table 3.3.2. The settling times are calculated as the difference in the time of minimal recorded position and first record of intended depth upon initial indentation of the graver. The graver was commanded independently of any other machine motions to obtain various depths. While the increments of 0.1 mm were minimal, the machine needed a

wide range of times to settle at its intended depth. Analysis of the settling time depicts the inconsistency in the timing of the IPF machine.

Table 3.4.2: Experimental Records of Settling Time

Indentation Depth (mm)	Graver Settling Time (s)
6.0	4.7
6.1	6.4
6.2	10.0
6.3	9.3
6.4	17.5

The large unpredictable range of settling times may be due to the fluctuation of the graver position over and under the intended depth due to machine limitations in the response of the indenter servo controls. The extended range of settling times is caused by the current position attempting to 'match' the commanded position but surpassing it by fractions of a millimeter either while increasing or decreasing position. The large variation in settling times is one example of the inconsistency with the timing of this machine.

Thus, the servo dynamic model cannot be validated using the experimental data collected. The times of initiation and completion of the gravers' position command during indentation are uncertain due to the timing issues related to the logic of the machine controls as mentioned within sections 3.3.1 and 3.3.2.

3.4.3 Unloaded contour scan limitation

The experiment described in section 3.2.4 posed an issue with scanning a contour of the unloaded tube after the long 500 mm groove was created. The extensive length created significant curvature in the tube. The curvature created issues in scanning the unloaded contour by the mounted Micro Epsilon unit. The Micro Epsilon scanner is restricted to a limited available scanning area, and therefore the contour was scanned with a weight applied at the end of the tube, as well as a support tool engaged, see Fig. 3.4.3.1.

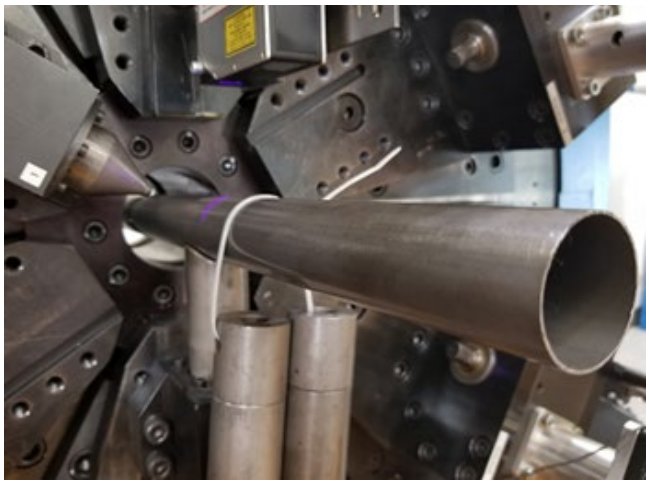

Figure 3.4.3.1 Contour scan with weights and tool support

Using the method depicted, Fig. 3.2.4.1 could be created. These accommodations were necessary to scan the tube at a constant and acceptable distance away from the Micro Epsilon scanner. However, these accommodations do not accurately represent the tube in an unstressed state. Observations of tube curvature during long grooving procedures provide evidence that the machine has limited ability to measure a groove contour of extensive length.

3.4.4 Inconsistent force measurement between operations

Within the experiments conducted, force data was gathered and did not depict consistent trends, as noted in Section 3.2.4. The difference in the total force measured could be a result of variation in forces other than grooving and support forces exerted on the tube by the IPF machine. In addition to the grooving and support forces, there are forces associated with the clamped portion at the hydraulic feed. Considering all forces acting on the tube, illustrated in Fig. 3.4.4.1, the forces measured by the piezoelectric force sensor may not be consistent between different grooving operations, if the clamping forces change.

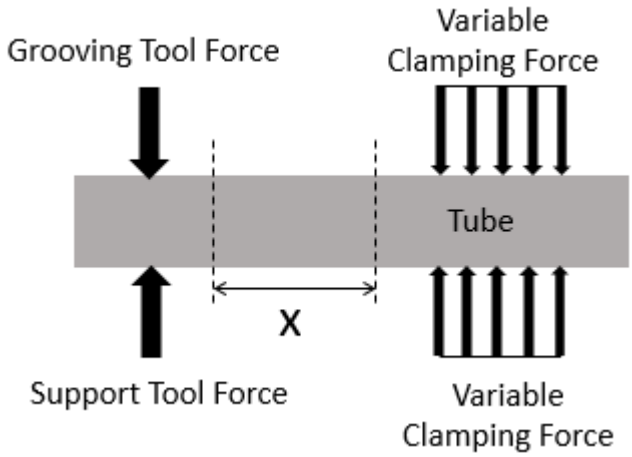

Figure 3.4.4.1 Free body diagram of tube with support and grooving tools engaged

As depicted above, the distance between the tools and the clamp, X, changes during the grooving procedure, leading to change in forces exerted at the tools. The manual clamping mechanism, as described

in section 3.1, can also changing moments each time it is secured around the tube. Thus, the inconsistency in force measurements, which were expected to increase linearly in Table 3.2.4, can be attributed to the clamping mechanism at the hydraulic feed, which allowed additional degrees of freedom as the bolts were secured around the tube manually. The distance from the contact point of the tools and the tube varied between each experiment as well, as the linear hydraulic actuator moved the clamp closer and further from the gravers. The potential variation in clamping the tube created inconsistencies in angle and position of the tube within the graving zone for different experimental runs.

3.4.5 Inconsistent force behavior between experimental setups

Prior experimental work by Grzancic (2017) has provided different insights into the radial force created due to grooving. The following experiment was conducted using the same 40 mm diameter E235 steel tube with 1 mm thickness. However, a 4 mm hemispherical tool radius was used instead of a 2 mm radius. As depicted below, there was strictly radial motion in the initial 4 seconds of the process, followed by strictly axial grooving. As shown in Fig. 3.4.5.1, there is a large peak of around 3000 N during radial indentation by the graver, and the radial force decreases during the axial motion.

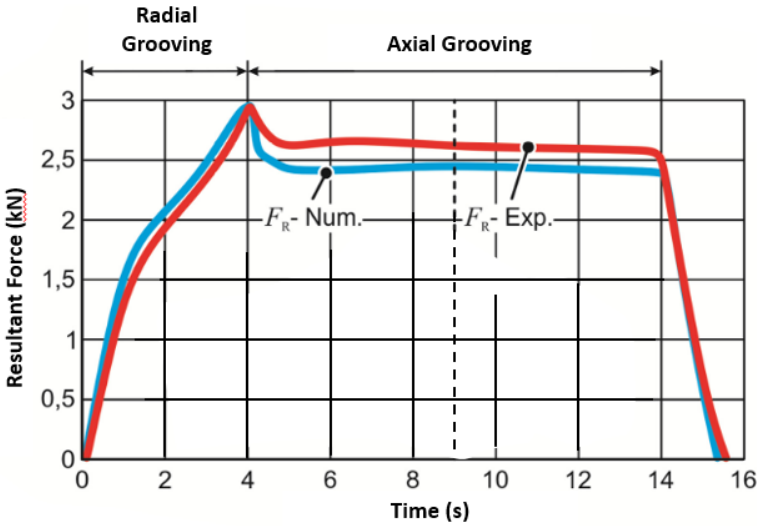

Figure 3.4.5.1 Prior experimental radial force data (Adapted from Grzancic, 2017)

Unlike the data collected above, the experimental work shown in both sections 3.2.5 and 3.3.2 do not replicate this effect. Furthermore, section 3.2.5 (radial indentation) and section 3.3.2 also show different radial force patterns from one another. The experiments all experience a strictly radial motion followed by a strictly axial motion, as Fig. 3.4.5.1 indicates. The difference is in the transition from the radial to axial grooving. The force decreases in the transition shown in Fig. 3.4.5.1, whereas the force increases in the transition shown in section 3.2.5, and remains the same in section 3.3.2. Thus, the method of force measurement is relevant. The documentation of the Kistler piezoelectric force sensor recommends a preloading of at least 20 % of its measuring range to mitigate the effects of bending moment. If there had been a preload supplied, the amount of compressive force on one side of the base of the tool would compensate for the amount of tensile stress on the opposite side due to the longitudinal motion and force of the tube created from axial grooving. The experimental setup used within this research did not validate a preload before experimentation, and so force data must be further investigated.

4 Preliminary Work in Active Stiffness Control and Online Identification

Experimental work has provided motivation for new control methods to be implemented into the current machine. Due to the IPF process's current state of susceptibility to geometry errors and the machine's high degree of flexibility, the new controls must support and accommodate a variety of grooving processes and tube materials. Analytical models of incremental profile forming that may be effectively used for controller design and implementation are central to the work described in this chapter, and are being formulated in parallel to this work. Two methods are investigated here, active stiffness control of tools that provide lateral support to the tube being indented as this may be used to achieve improved groove geometry accuracy, and online identification of material parameters to account for variations in related deformation behavior.

4.1 Active Stiffness Control

Previously collected experimental data motivates the implementation of active stiffness control of support tools that can modulate the lateral support of tubes processed by the IPF machine. The current servo dynamic model was used to help identify an appropriate method for active stiffness control. After confirmation of the nearly rigid support system under position control, active stiffness control was added to the IPF graver model which was developed in Chapter 2. The determination of the desired active stiffness of the lateral supports will depend upon the capability of models of the IPF process to predict the stiffness values that lead to improved accuracy of groove geometry. Currently, computationally simple models of the IPF process with this capability are lacking.

4.1.1 Motivation behind active stiffness control of IPF support gravers

The IPF process is a unique process that is capable of forming a great variety of tubular profiles. Through experimentation, IPF-processed tube contours were inspected. The pattern of geometry errors observed from these contours also suggests ways of improving profile accuracy. Potential control schemes were evaluated to redefine the IPF grooving process and help mitigate these geometric errors. Previously collected contours from past experiments provide the incentive for active stiffness control of the support tools.

A previously conducted experiment (Fig. 4.1.1.1) utilized two tool configurations: one in which no side support is provided (free) and the other in which both sides are supported (restricted). The two post-process unloaded contours vary significantly from one another, as well as from the targeted longitudinal groove depth of 4 mm.

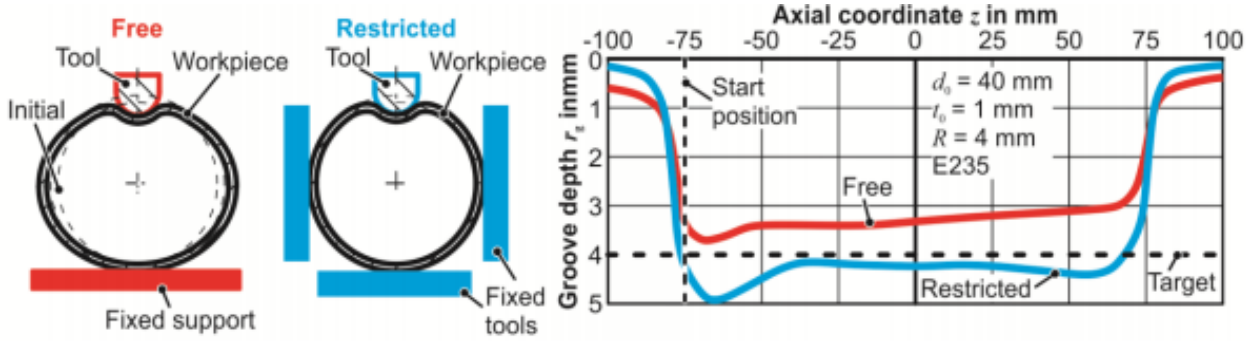

Figure 4.1.1.1 Groove contours with and without side supports (Srinivasan and Tekkaya, 2018)

The contour developed from the free setup demonstrates significant elastic springback of the tube material, while the restricted setup demonstrates less elastic deformation and springback. The desired depth of 4 mm lies between both contours created from the free and restricted configurations. Thus, modulation of the support stiffness between the free and restricted setups could result in a consistent groove contour of 4 mm if the side support stiffness were manipulated appropriately. A variable stiffness in between compliant and rigid supports could create the necessary combination of the two configurations, in which the free setup is representative of side supports with zero stiffness, and the restricted setup is representative of rigid side supports having an infinite stiffness. The process could be modified to imitate compliance closer to the free-setup during initial indentation, and tend to a more rigid support, like the restricted-setup, during axial grooving. Prior to this work, stiffness of a "fixed tool" was unknown. The side supports were assumed to be infinitely stiff or act as rigid supports. Thus, the actual stiffness of the gravers needed to be determined.

4.1.2 Determination of the stiffness of the model developed

The stiffness of the tools must be calculated to confirm the rigidity of the "fixed" side supports. Analysis of the stiffness was determined from the model developed in Chapter 2. The stiffness is computed from the change in position of the graver given an external radial force acting at the graver. The following block diagram was manipulated and reduced to result in a transfer function of motor position rotation over an input of load torque. A few reductions are captured in Figs. 4.1.2.1 - 4.1.2.4.

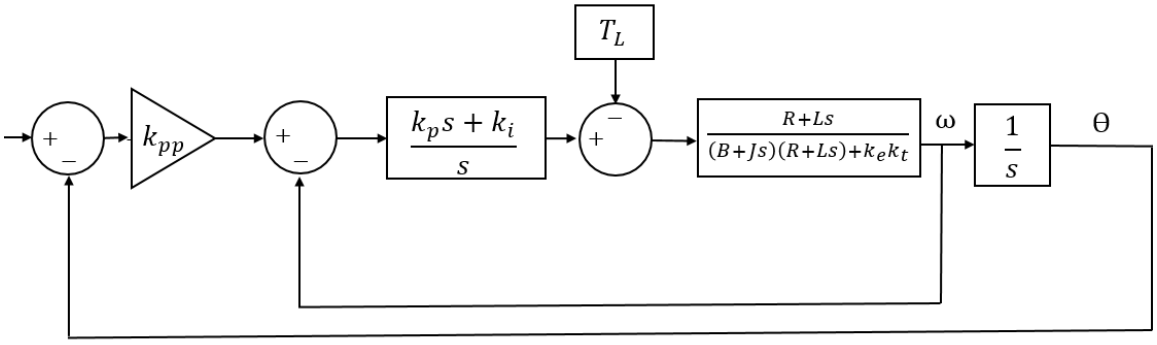

Figure 4.1.2.1 Block diagram reduction for determination of stiffness

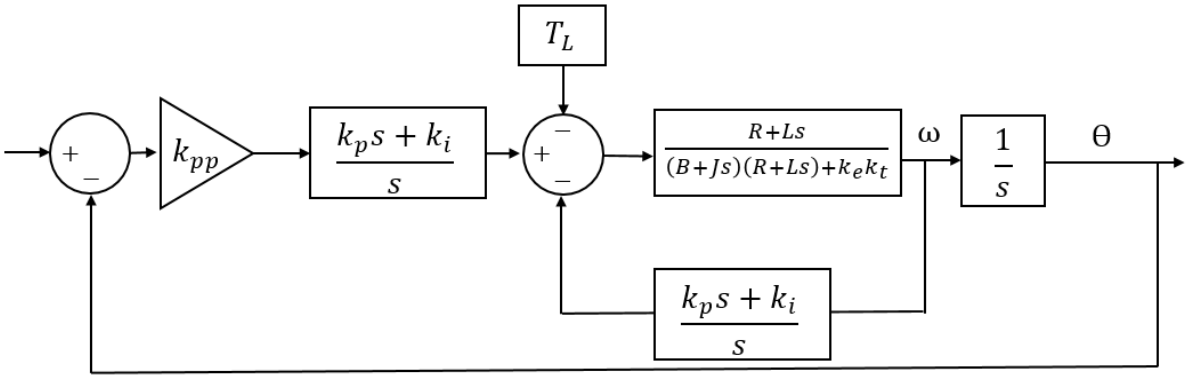

Figure 4.1.2.2 Second iteration of block diagram reduction for determination of stiffness

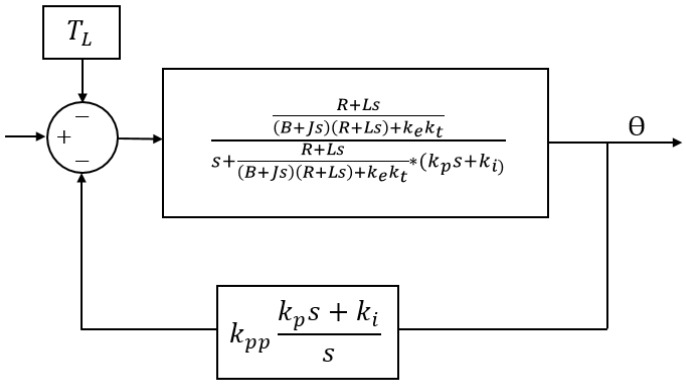

Figure 4.1.2.3 Third iteration of block diagram reduction for determination of stiffness

The transfer function of $\frac{\theta_{out}}{T_L}$ was determined from the block reduction.

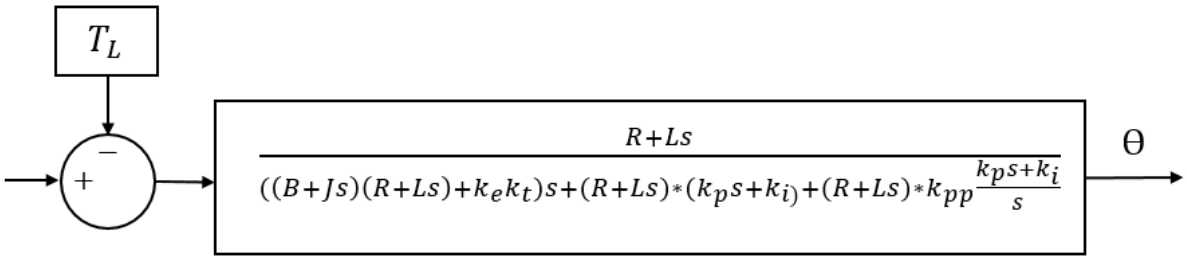

Figure 4.1.2.4: Fourth iteration of block diagram reduction for determination of stiffness

The transfer function can be rewritten as:

$$\frac{\theta_{out}}{T_L}=\frac{(R+Ls)s}{LJs^4+(RJ+LB+k_pL)s^3+(RB+Rk_p+Lk_i+Lk_{pp}k_p+k_tk_e)s^2+(Rk_{pp}k_p+Rk_i+Lk_{pp}k_i)s+Rk_{pp}k_i} \quad [4.1.2.1]$$

The steady state stiffness is calculated as the limit of [4.1.2.1] is taken as s tends to zero, so that the following relation can be calculated numerically.

$$\frac{\theta_{out}}{T_L}=0\ [\frac{rad}{N.m}] \quad [4.1.2.2]$$

Thus, the change in graver position would be zero and depicts that the system model is very stiff. The assumption of the rigid support tools, as depicted in Grzancic's work, is confirmed: the tools have a very high stiffness.

4.1.3 Addition of stiffness control to model

Since the rigidity of the tools is so great, a control scheme can be created to command an adjustment of position to the machine gravers based upon the force load supplied to them. A gain of a stiffness constant

would continue to be varied during grooving to designate a position for the support tool given the current value of the force applied to it. So, a requirement of this approach to active stiffness control is that the force must be sensed in order to determine the motion to be commanded.

For simulation purposes, an input of torque at the motor is assumed, to determine how much to vary the stiffness. During indentation, the stiffness can be varied using the stiffness constant, k_v, as described in the block diagram below:

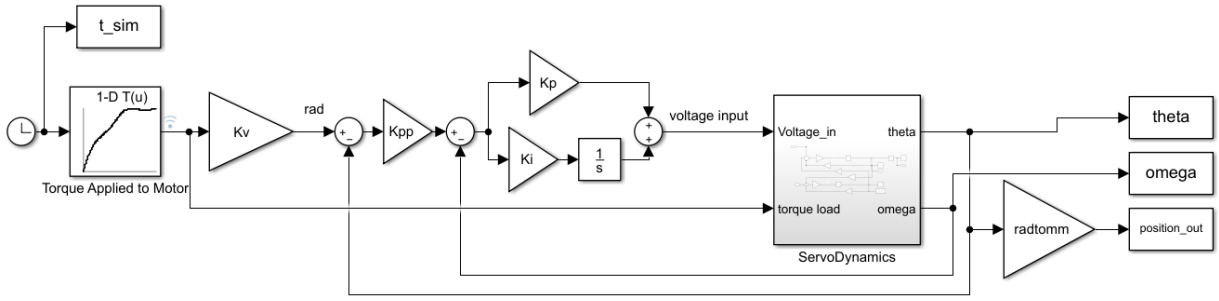

Figure 4.1.3.1 Active stiffness control Simulink block diagram

An input of torque was recreated from experimentally measured force data at the grooving tool during indentation of the graver to a depth of 6 mm at 1 mm/s. The force in Fig. 4.1.3.2 is not an accurate depiction of the force acting on the side supports, it is for demonstration purposes only and is assumed representative of a side support force. Force measurement of side supports can be gathered in future experiments to help implement active stiffness control.

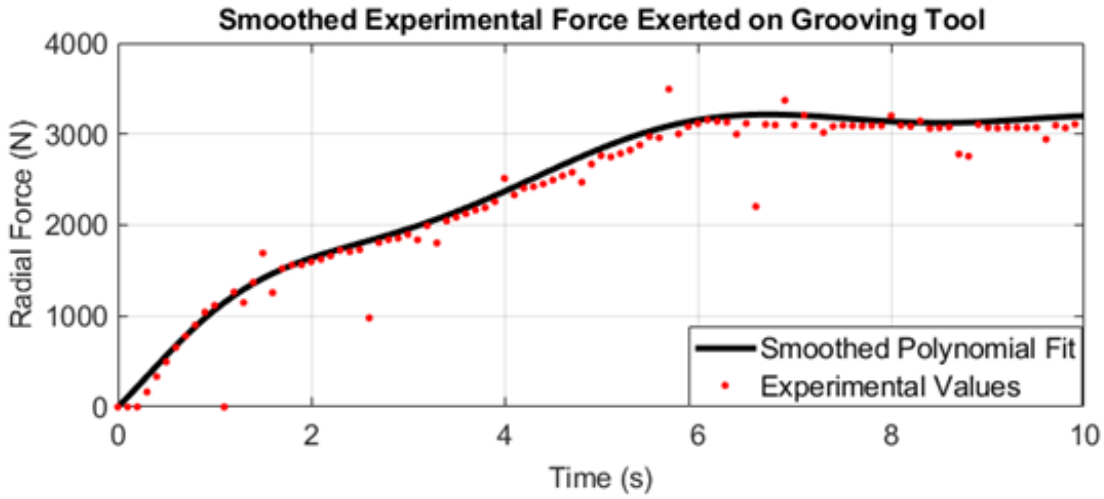

Figure 4.1.3.2 Radial force for determination of side support servo command

Various stiffness constants can be utilized to adjust the position of the graver as the force on the side support either increases or decreases during graving. Assuming a stiffness constant of -5 rad/Nm, the side support would retract itself from the tube material, leaving the tube more area to expand. Fig. 4.1.3.3 shows the commanded position to the side support servo for the force trajectory in Fig. 4.1.3.2.

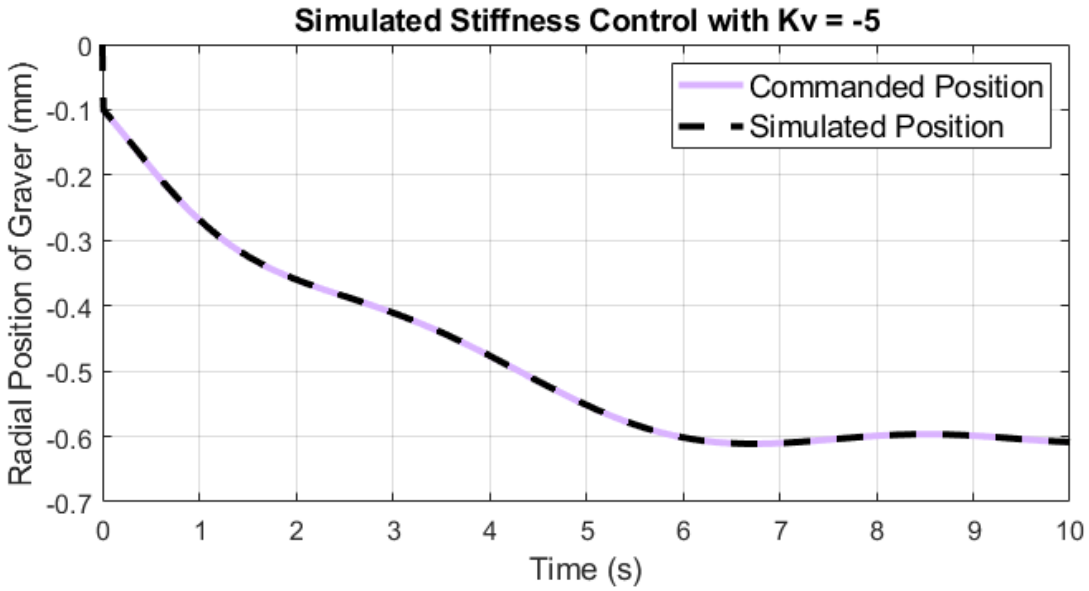

Figure 4.1.3.3: Simulated stiffness control with constant k_v

Physical models of tube deformation would need to be created to see how the sides bulge for a given force, and how the force would need to be handled on the sides to create the desired groove contour. Although the above simulation models stiffness control, it does not simulate active stiffness control. Active stiffness control would incorporate a continuously changing stiffness constant to aid in successful grooving. For example, at the beginning of grooving, we could use a larger stiffness gain, to create a more compliant side support, and then decrease the stiffness gain to obtain a more rigid support during axial grooving. A simple representation of active stiffness control was created in which the initial k_v value was -10 $rad/N.m$, and at 4 seconds decreased in magnitude to -2 $rad/N.m$. The same force plotted in Fig. 4.1.3.2 was assumed in the following active stiffness simulation with a shifting k_v.

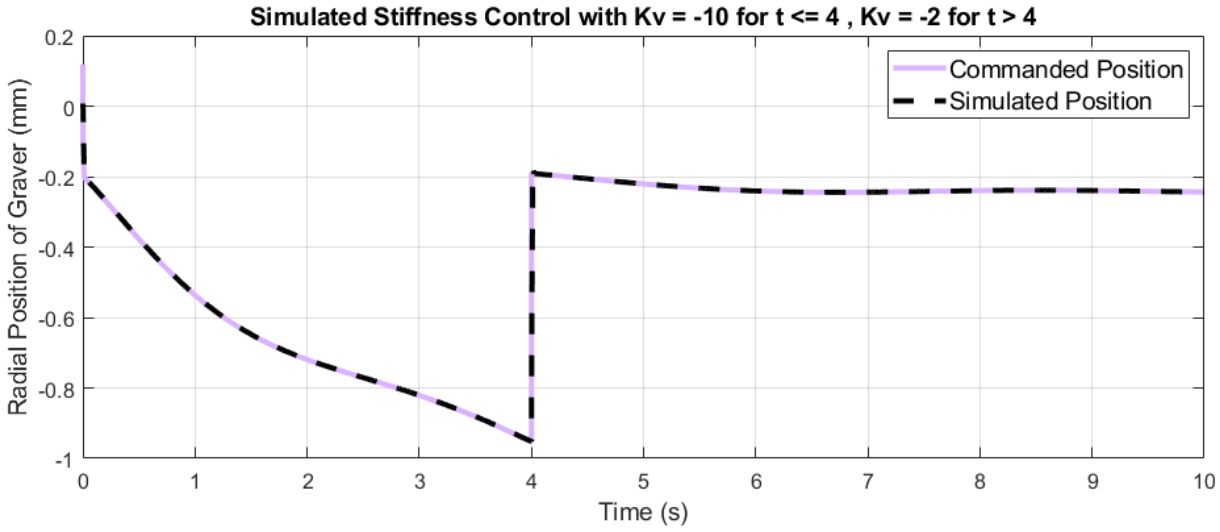

Figure 4.1.3.4: Simulated stiffness control with varying k_v

The plot above exhibits a potential change in compliance that could be applicable to the IPF grooving process, to decrease the stiffness upon radial motion, and increase during axial grooving. With a varying stiffness gain, the side support tools could adjust themselves at all times to resemble a rigid or compliant support or one in between.

4.2 Online Identification of material model parameters

Currently, a commanded groove depth cannot be precisely executed due to a variety of material deformation phenomena which occur during radial grooving. Phenomena such as elastic springback and plastic bulging result in actual contour deviation from the intended contour. Reconfigured tool trajectories and adjusted tool stiffness are two methods that could diminish the effect of these undesirable material behaviors. However, the amount of springback and bulging could vary from one part to the next due to variations in material model parameters, such as elastic modulus or flow stress. During the process, the material behavior of tube is examined to change. The motivation of online identification is to detect changes in material behavior for the same material during grooving.

Thus, the process control must be changed from part to part to help mitigate the effect of changes in material model parameters as these are unavailable to the IPF machine controls. Online identification was recognized as an applicable control scheme for the IPF machine so that these cases can be accommodated. Online identification could capture information of the tube material properties during radial grooving to then adjust the control of the next part accordingly to mitigate the effect on profile geometry.

4.2.1 Assumptions for tube deformation formulation

A model of the mechanics behind the material deformation due to the radial grooving of the IPF process is being formulated. The formulation describes the radial force acting at the graver for a specified radial indentation value through a known material property, flow stress (S. Seetharaman, personal communication, 2019). The application of this formulation will be beneficial as indentation depth of the graver and radial force exerted on the graver can both be measured within the current setup of the IPF machine. Provided radial force and indentation, the flow stress of a material during processing can be calculated using the current formulation of the mechanics of the IPF graver indentation process.

The model, however, has limitations and does not capture the true mechanics of the indentation. The model is restricted to purely radial motion of the graver. The modeled tube is represented as a rigidly plastic model, whereas the true indentation process develops strain hardening in the tube, as well as other elastoplastic effects. Therefore, the model cannot be expected to accurately resemble results found from experimentation. The formulation is empirically observed to only be valid for a limited range of tool indentation values.

A crescent-shaped support is considered where its central point of contact with the tube material is assumed fixed. The formulation also models the grooving tool as a point load, and thus the model is insensitive to tool geometry. The tube is modeled by a set of rings accounting for cross-sectional deformation and generators accounting for deformation along its longitudinal axis. The sum of the dissipation of internal energy from ring crushing, represented by plastic hinges, and generator stretching, represented by axial membranes, was equated to the rate of work of the external force. Given a specified

tube material and a known radial tool position, the radial force at the graver can be calculated from this formulation.

The assumptions and methods describing the formulation can be summed up and simplified, for the purpose of this research, into the equation [4.2.1.1]. The radial force, P , in Newtons, is a function of the flow stress, σ, in MPa, and $f(\delta)$, a function developed using the model described above, indentation depth δ in mm. The flow stress remains constant for each material.

$$P = \sigma * f(\delta) \quad [4.2.1.1]$$

4.2.2 Prediction of flow stress from experimental data

The equation was rearranged to predict flow stress given an experimentally determined force and tool position.

$$\sigma = P / f(\delta) \quad [4.2.2.1]$$

Experimental measurements of radial force and position using E235 steel, 6060 aluminum alloy, and 800 dual phase steel tubes were gathered from previous works. The following data represents a 6 mm indentation of pure radial motion commanded to the grooving tool. Force data was then smoothed using a third order least-squares polynomial fit. The flow stress computed using equation [4.2.2.1] and experimental data is then compared to the flow stress of the material determined experimentally using standard approaches in material testing.

The first plot in Fig. 4.2.2.1 shows experimental and modeled radial force versus tool position for E235 steel with a flow stress of 650 MPa. Fig. 4.2 depicts the calculated flow stress using equation [4.2.2.1] from the measured/modeled radial forces and tool positions.

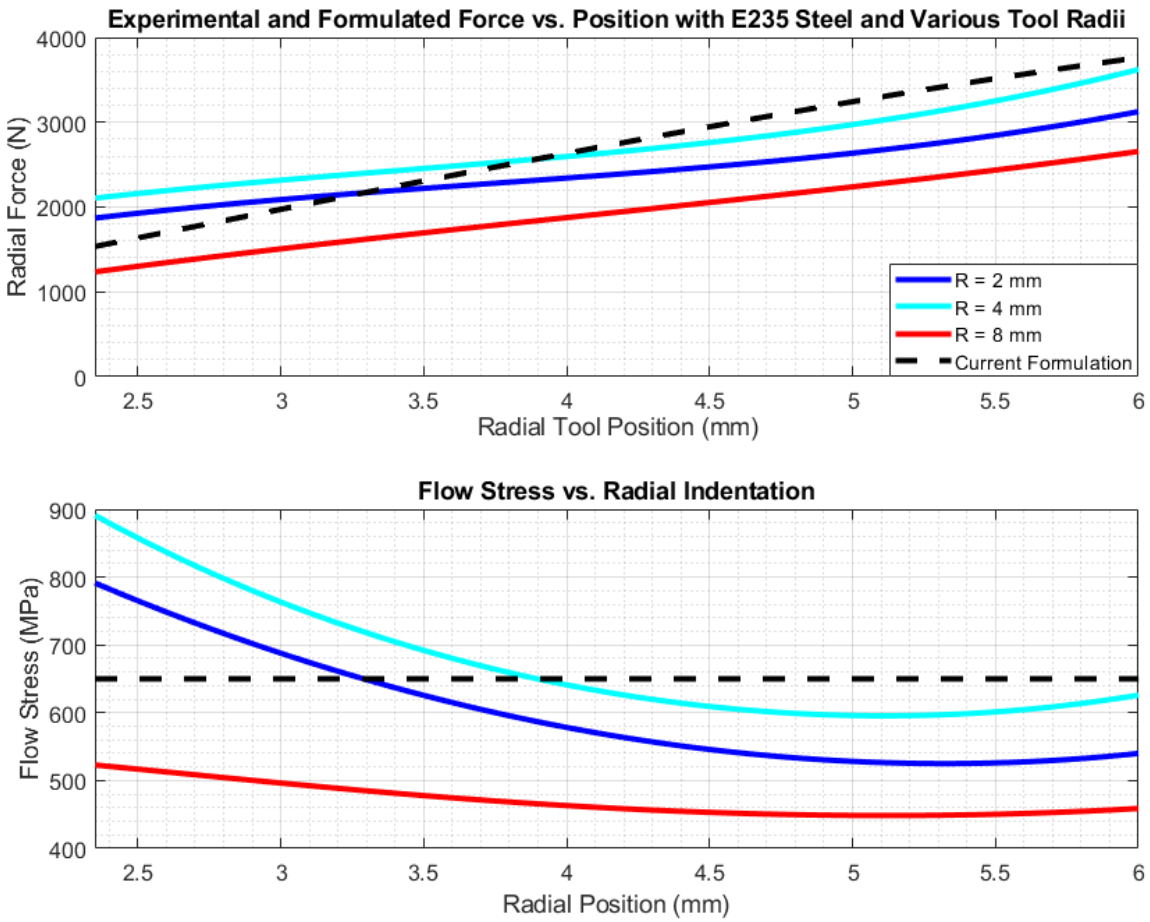

Figure 4.2.2.1 Calculated and formulated flow stress of E235 steel

The figures above depict the large range of calculated flow stress from the three experiments with three various hemispherical tool radii, R. The deviations in these plots represent phenomena in the grooving process that are not represented in the current analytical formulation. Sensitivity to tool geometry and the addition of elastic plastic modeling of the process are two assumptions that must be re-evaluated to improve the correlation between flow stress and grooving mechanics. The point load model creates no distinction between the 2 mm and the 8 mm tool radius indentation, while the experimental results show the distinct variation in the two. Further, curvature in the flow stress lines is apparent within all tool radii, which the constant value of the flow stress of the model does not capture. The curvature in the plots may also be due to elastoplastic behavior of the tube material that is not captured within the model.

Flow stress calculations from experimental measurements for other materials were also examined. 6060 aluminum alloy, Al6060, and 800 dual phase steel, DP800, with flow stress values of 191 MPa and 615 MPa, respectively, are inspected in the plots below (Figs. 4.2.1.2 and 4.2.1.3). The deviations between experimental and modeled flow stress for each material depict the range of error associated with prediction of each material with the current formulation. As the formulation becomes more refined to simulate tube grooving, the percentage of error between model and experimental flow stress will decrease. To distinguish material parameters due to the way the material was preprocessed, differences of

a few percent of the flow stress values are necessary. Currently, however, various materials are compared to validate if this method is capable of capturing a large difference in material parameters, as it is preliminary work. Fig. 4.2.1.2 replicates curvature similar to that seen with the E235 steel data.

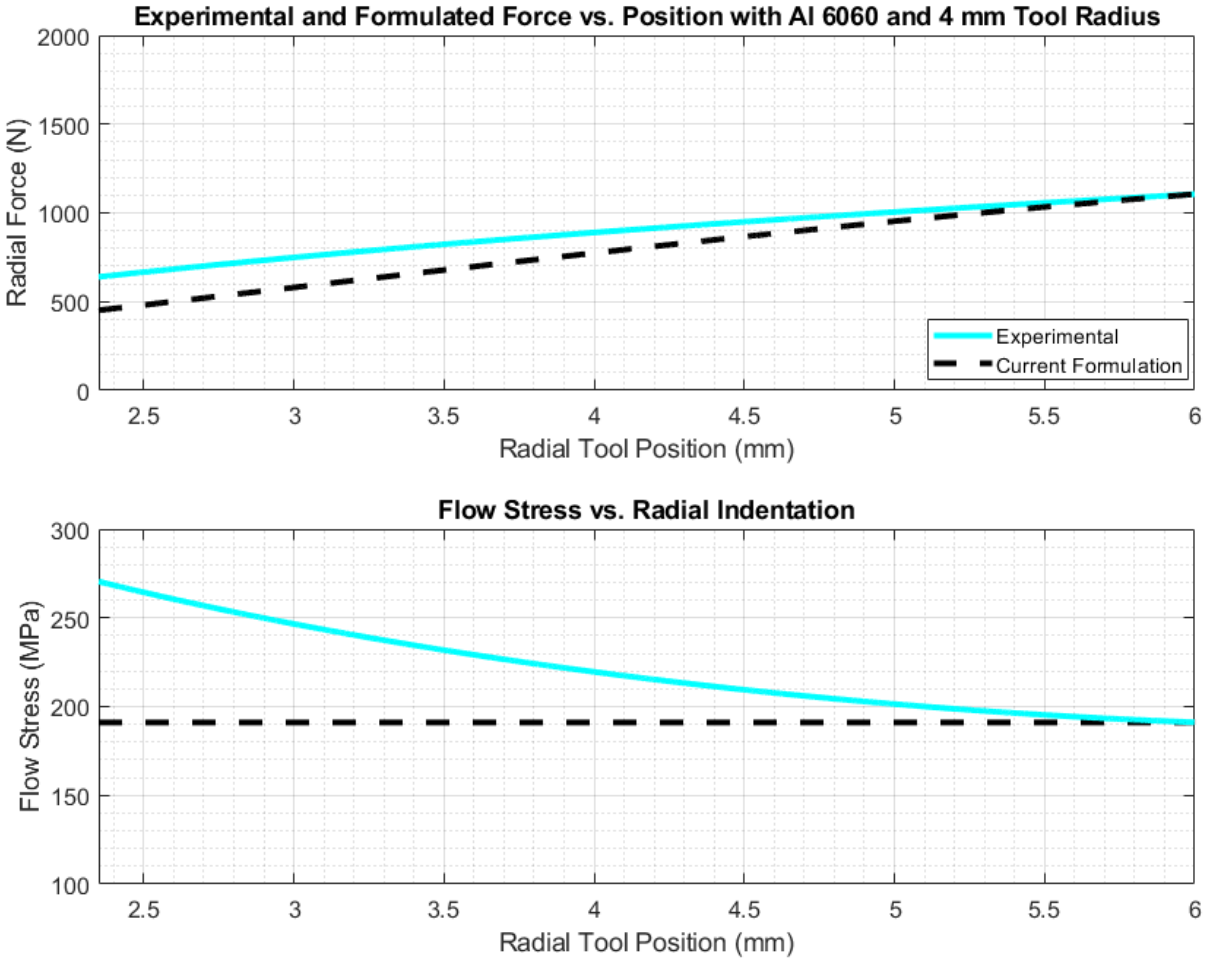

Figure 4.2.1.2 Calculated and formulated flow stress of Al 6060

Although the values of flow stress calculated stray from the anticipated flow stress of the specified material, the difference between modeled and experimental flow stress of 6060 aluminum alloy is around 80 MPa. Thus, the large difference between E235 steel and Al 6060 can be captured with this formulation since the flow stress of the two materials varies greatly. However, the error will need to be within a few percentage to capture a single material's parameter variation due to preprocessing. The last material used in experimentation has a similar expected flow stress value to steel E235, and therefore could not be differentiated with the current method. Again, the curvature of DP800 (Fig. 4.2.1.3) follows a similar curvature seen within E235 and Al6060.

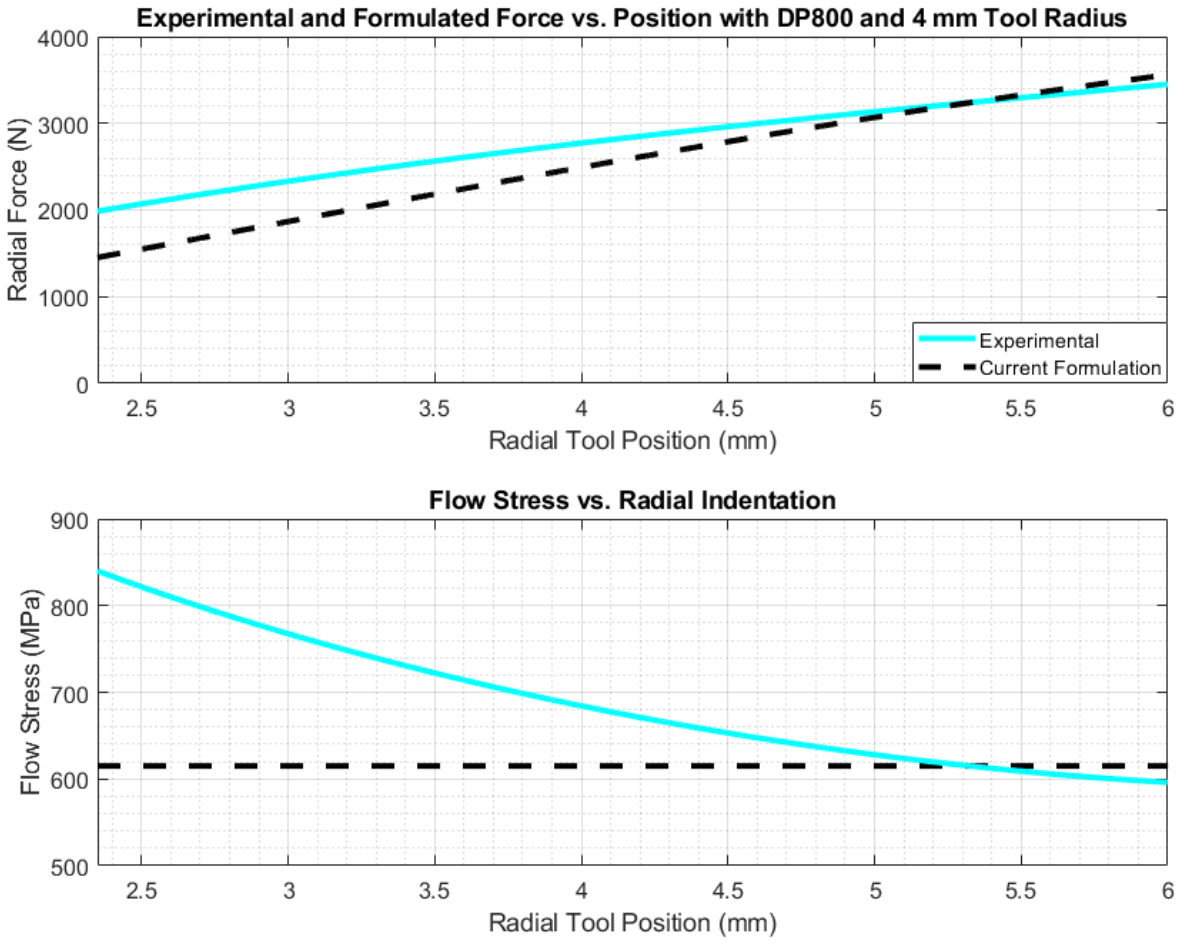

Figure 4.2.1.3: Calculated and formulated flow stress of DP800

Thus, further work involving the model of the grooving process needs to be done to capture tool geometries as well as true elasto-plastic behavior of the tube material during indentation.

5 Chapter 5: Conclusions and Future Recommendations

A model of the IPF machine gravers was established in Simulink. The detailed model of the IPF machine needs to be refined for future simulations. Due to incomplete documentation of control parameters, new controller gains were designed and assigned within a similar feedback loop configuration. Thus, the model depicted in Chapter 2 is representative of the actual IPF machine graver dynamics but is not based completely upon the experimental system. Therefore, before future experiments are conducted and any other control manipulations are made, the current machine gravers should be adapted to match the developed model to assure experiments can be compared with actual machine dynamics.

Experiments conducted within this work revealed details of IPF behavior in response to commands that were problematic. The experimental work also depicted timing inconsistencies within the machine graver controls. Control modification can help eliminate these timing inconsistencies. Then, model validation would be possible presumably without the current controller logic which delays command execution. Transparent controller information, as well as consistent execution of commands, will enable the comparison needed between the actual IPF machine and the model.

To model the entire IPF process in its current state, system dynamics and controller information of all 8 degrees of motion will need to be captured. Thus, the modeling and experimental validation will have to be extended to both the rotary disk and the hydraulic feed. Only after all degrees of motion are captured in a model can the IPF process be wholly recognized and understood. Only then are further modification and testing of control schemes discussed appropriate.

Before implementation of either of the two control schemes, active stiffness control and online identification, can be addressed, issues related to measurement of external forces acting on the tools must be accurately recognized. Experimental work involving force measurements should be re-evaluated with a monitored installation procedure. Also, measurements of current to the graver should be evaluated through the system for comparison. Only then can force measurements, which are needed by both active stiffness control and online identification, be pursued.

Active stiffness control was evaluated in an effort to emulate a process setup with compliant side supports. After the modifications and concerns noted above are accommodated, active stiffness control should be implemented within the supports of the actual machine. Experiments similar to those conducted at TUD using free versus restricted lateral supports should be conducted with the addition of active stiffness control and contour data collected. The stiffness should be modified for each design and parameters should be identified to best improve accuracy of contour geometry. Efforts to successfully identify optimal stiffness control for different materials and part geometries should be considered.

Online identification efforts need to be continued as a final step. The current formulation for flow stress identification is limited as it represents only rigid-perfectly plastic material behavior. Thus, the current formulation needs to be reconstructed to capture elastoplastic behavior of the material. Further, more experiments resulting in force data will need to be collected to successfully identify flow stress and other material model parameters.

References

[1] Allwood, J.M., Duncan, S.R., Cao, Groche, J.P., Hirt, G., Kinsey, B., Kuboki, T., Liewald, M., Sterzing A., Tekkaya, A.E., 2016, “Closed-loop control of product properties in metal forming”, CIRP Annals - Manufacturing Technology

[2] ANT Antriebstechnik, 2019, “Produktbeschreibung 1, Spindelhubgetriebe”

[3] Grzancic G., 2017, “Verfahrensentwicklung und Grundlagenuntersuchungen zum Inkrementellen Profilumformen”

[4] Grzancic G. et al., 2014, "Innovative Machine Design for Incremental Profile Forming", Key Engineering Materials, Vols. 622-623, pp. 413-419

[5] Kistler Group, 2009, “SlimLine Sensors (SLS) – Measurement of Dynamic and Quasistatic Forces, 0 … 3 kN up to 0 … 80 kN, Type 9130B… up to 9137B…”

[6] Moreton, P., 1999, *Industrial Brushless Servomotors,* Newnes, Woburn, MA

[7] Mott, R., 1985, *Machine Elements in Mechanical Design,* Pearson Prentice Hall, Upper Saddle River, NJ

[8] Seetharaman, S., 2019, personal communication

[9] Srinivasan K. and Tekkaya A.E., 2018, “Closed Loop Control of Innovative Incremental Profile Forming,” Proposal Submission

[10] Tibor, B. et al., 2011, “Modeling and Simulation of the BLDC Motor in MATLAB GUI”

[11] Yedamale, P., Microchip Technology Inc., 2003, “Brushless DC Motor Fundamentals”

Appendix

A1. Simulink Diagrams

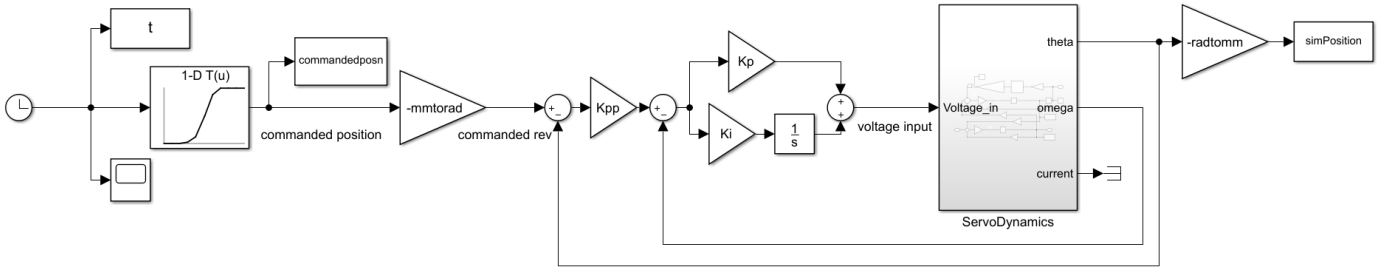

Figure A1.1: Simplified BLDC model

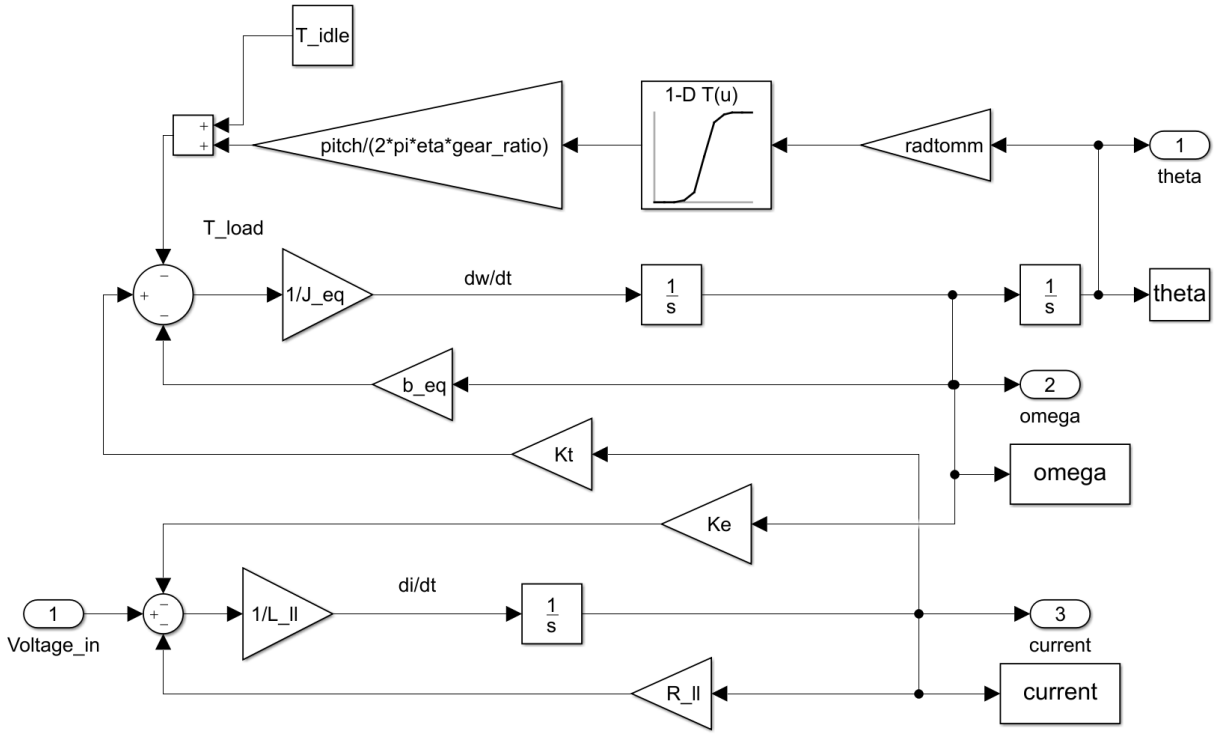

Figure A1.2: Simplified BLDC motor dynamics model

A2. Matlab

Chapter 2 - Modeling Calculations
Dynamic Model of Brushless Motor

```
% Motor Constants
J_m = 2.19 / 100^2;             % kg.m^2 % Motor inertia
b_m = 0.355;                    % N.m.s/rad % Motor damping ratio
L_uv = 17.906*10^-3;             %henrys % motor winding inductance per phase
R_uv = 17.874;                  %ohms % motor winding resistance per phase
Ke_pk = 135.88;                 %mV*min % phase to phase peak emf constant

% Inductance
% Equation 2.1.1
```

```
L_ll = 2*L_uv;                  %henrys % motor winding line to line inductance

% Resistance
% Equation 2.1.2
R_ll = 2*R_uv;                  %ohms % motor winding line to line resistance

% EMF Constant
Ke_pk_conv = Ke_pk*60/(1000);   %V-s % phase to phase peak emf constant
% Equation 2.1.3
Ke_eff = Ke_pk_conv/sqrt(2);    %V-s % effective emf constant
% Equation 2.1.4
Ke = sqrt(3)*Ke_eff;            %V-s % rms emf line to line


% Torque Constant
% Equation 2.1.5
Kt = sqrt(3)*Ke;                % Nm/A_rms % Torque constant
```

Mechanical Transmission System Model

```
% Constants
N = 6;                                  % Gear ratio

% graver
l_graver = 0.4;                         % m % length of graver
d_graver = 0.039;                       % m % diameter of graver base
rho_graver = 7715;                      % kg/m^3 % density of graver
m_graver = rho_graver * l_graver * ...
    (pi/4) * d_graver^2;                % kg % mass of graver

% lead screw
density_ls = 0.0114*1000;               % kg/m % density of lead screw
l_ls = 0.08;                            % m % length of lead screw
d_ls = 0.03;                            % m % diameter of lead screw
m_ls = density_ls*l_ls;                 % kg % Mass of lead screw
p_ls = 5e-3;                            % m/rev % pitch with rotation of lead
screw

% Rotational Inertia of the Lead Screw
% Equation 2.2.1.4
J_ls_rot = 0.5 * m_ls * (d_ls/2)^2;     % kg.m^2 % Rotational inertia of lead
screw

% Inertia of Graver and Lead Screw
% Equation 2.2.1.6
J_graverandscrew = (m_graver+m_ls)*...
    (p_ls/(2*pi))^2 + J_ls_rot;         % kg.m^2 % Inertia of screw and graver

% Equivalent Inertia at Motor
% Equation 2.2.1.10
J_eq = J_m + J_graverandscrew/N^2;      % kg.m^2 % Equivalent inertia
```

```
% Damping
b_gear = 0.01;                                  % N.m.s/rad % Damping ratio of gear mesh

% Equivalent Damping Ratio at Motor
% Equation 2.2.2.6
b_eq = b_m + b_gear*(1+(1/N)^2);                % N.m.s/rad % Equivalent damping ratio
```

Model Input of User to Tool Position of Graver

```
% Programmable Variables:
% depth of groove, length of groove

% Predetermined variables:
% Acceleration time of graver set by KEB = 0.2 s
% Deceleration time of graver set by KEB = 0.1 s

% Define depth of graver
prompt = 'Depth of Groove (mm) : ';
depth = input(prompt);

% Create piecewise function
syms t                                      % seconds % create symbol t = time
V_graver = 1;                               % set graver speed %1 mm/s
depth = depth;                              % mm
V_hydfeed = 5;                              % set hydraulic feed speed %mm/s
position(t) = piecewise( ...
0<= t <=0.2, -0.5*5*(t)^2, ...
0.2 < t <= depth + .05 , -t + 0.1 , ...% where 0.1 = -0.5*5*(.2)^2
depth + .05 < t <= depth + 0.15,  0.5*10*(t - (depth + 0.05))^2  - t + 0.1, ...
depth+0.15<=t, -depth);


% Plot  Commanded Position
figure(1)
fplot(position, '-r', 'LineWidth', 3)
xlim([0, depth + 5])
ylim([-depth-1, 0.5])
xlabel(['\fontsize{16}Time (s)'])
ylabel(['\fontsize{16}Position of Graver (mm)'])
title(['\fontsize{16}Commanded Graver Trajectory vs. Time'])
```

Design of Gains

Determine Kp and Ki of Velocity Loop

```
% Motor transfer function and values
% Equation 2.3.2.1
num = [Kt];
den = [L_ll*J_eq, R_ll*J_eq+L_ll*b_eq, Ke*Kt+R_ll*b_eq];
openVelLoop = tf(num, den);
```

```
% Run Control System Designer
controlSystemDesigner(openVelLoop)
% Ki and Kp values determined
Ki = 8699.6;                        % Integral Gain
Kp = 7.2076;                        % Proportional Gain
```

Determine Kpp of Position Loop

```
% Equation 2.3.2.2
num = [Kt*Kp, Ki*Kt];
den = [L_ll*J_eq, R_ll*J_eq+L_ll*b_eq, Ke*Kt+R_ll*b_eq+Kt*Kp, Ki*Kt, 0];
openPosnLoop = tf(num, den);

% Run Control System Designer
controlSystemDesigner(openPosnLoop)
% Kpp determined
Kpp = 313;
```

Plot Closed Loop System Response

```
% Equation 2.3.2.3
num = [Kp*Kt*Kpp, Ki*Kt*Kpp];
den = [L_ll*J_eq, R_ll*J_eq+L_ll*b_eq,
Ke*Kt+R_ll*b_eq+Kt*Kp,Kp*Kt*Kpp+Ki*Kt,Ki*Kt*Kpp];
sys = tf(num,den);

% Plot Step response
step(sys)
% Determine bandwidth
bw = bandwidth(sys);
% Bode Plot
bode(sys)
```